Journal of Marine Systems 204 (2020) 103292

Contents lists available at ScienceDirect

Journal of Marine Systems

journal homepage: www.elsevier.com/locate/jmarsys

Influence of suspended sediment front on nutrients and phytoplankton dynamics off the Changjiang Estuary: A FVCOM-ERSEM coupled model experiment

Jianzhong Ge[a,b,*], Ricardo Torres[c], Changsheng Chen[d], Jie Liu[e], Yi Xu[a], Richard Bellerby[a,f], Fang Shen[a], Jorn Bruggeman[c], Pingxing Ding[a]

[a] State Key Laboratory of Estuarine and Coastal Research, East China Normal University, Shanghai 200062, China
[b] Institute of Eco-Chongming, No.20 Cuiniao Road, Chenjiazhen, Shanghai 202162, China
[c] Marine Ecosystems Models & Predictions, Plymouth Marine Laboratory, Prospect Place, The Hoe, Plymouth PL1 3DH, UK
[d] School for Marine Science and Technology, University of Massachusetts-Dartmouth, New Bedford, MA 02744, United States
[e] Department of Biological Sciences, University of Bergen, Postbox 7803, N-5020 Bergen, Norway
[f] Norwegian Institute for Water Research, Thormølensgate 53D, N-5006 Bergen, Norway

ARTICLE INFO

Keywords:
Phytoplankton
Nutrients
Changjiang Estuary
Sediment front

ABSTRACT

High-turbidity water is a common feature in the estuary and inner shelf. Sediment suspension functions as a modulator that directly influences the interactions among nutrients, phytoplankton and other related ecosystem variables. A physical-biological coupling model system was applied to examine the impact of sediment front on interactions among on suspended sediment, vertical mixing, nutrients and phytoplankton over the inner shelf off the high-turbidity, phosphate-limited Changjiang Estuary. The physical model was the Finite-Volume Community Ocean Model (FVCOM) and the biological model was the European Regional Seas Ecosystem Model (ERSEM). Results revealed that in the nearshore region the growth of phytoplankton over the spring-summer seasons was limited by suspended sediments and intensified vertical mixing during the autumn-winter seasons extended the sediment-induced suppression extended offshore to restrict the phytoplankton growth over the shelf. Nutrients were diluted by spreading of freshwater discharge and significantly decreased off the suspended sediment front due to the depletion by the offshore phytoplankton growth. The simulation results showed that although the diatom phytoplankton dominated the Chlorophyll *a* (Chl-*a*) concentration, the non-diatom group had a more contribution to the biomass. The relatively high phytoplankton biomass was found over the offshore deep underwater valley area as results of remote advection by the Taiwan Warm Current and weak turbulent mixing.

1. Introduction

Estuaries are highly productive system in which physical, biogeochemical and ecological processes strongly interact. Dissolved and particulate matters (organic and inorganic), including nitrogen (N), phosphorus (P), silicon (Si) and carbon (C), enter the estuary through upstream rivers, point discharges from human wastewater, and non-point fluxes from the land along the coast as well as submarine groundwaters (Sadat-Noori et al., 2016; Moore, 2006, 2010). In an estuary, the growth of phytoplankton is controlled by the abiotic and biotic components in the nutrient cycles of the ecosystem (Klausmeier et al., 2008). Nutrient loadings from various sources make an estuary become a nutrient-rich ecosystem, where abundant supplies of nutrients greatly impact biological productivity.

Suspended sediment is a common feature in estuaries. In a high-turbidity region, sediment resuspension has a great impact on nutrient cycles and phytoplankton community (Kang et al., 2012; Franklin et al., 2018). On the biological level, resuspension activates the nutrient exchange between the water column and bottom benthic layer, and hence enhances the non-diatom plankton growth in the water column (Chen et al., 2004; Boynton et al., 2018). On a physical level, suspended particulate sediments reduce light penetration in the water column. In a high-turbidity environment, the phytoplankton growth is light limited. Increasing light attenuation coefficient limit the photosynthesis process and thus primary production in a nutrient-rich region (Ji et al., 2002; Chen et al., 2004; Vanderploeg et al., 2007; Donohue and Garcia

---

[*] Corresponding author at: State Key Laboratory of Estuarine and Coastal Research, East China Normal University, Shanghai 200062, China.
E-mail address: jzge@sklec.ecnu.edu.cn (J. Ge).

https://doi.org/10.1016/j.jmarsys.2019.103292
Received 13 July 2019; Received in revised form 13 November 2019; Accepted 15 December 2019

Molinos, 2009; Sobolev et al., 2009; Huettel et al., 2014; Hu et al., 2016; He et al., 2017; Niemistö et al., 2018).

Previous observational and modeling studies have already confirmed the inhibition of suspended sediment on phytoplankton growth in the suspended sediment plume in the Changjiang Estuary (Zhu et al., 2009; Wang et al., 2019). In this estuary, however, a sediment plume usually co-occurs with a dissolved nutrient plume as well as a low-salinity plume (Chen et al., 2003b; Ge et al., 2015b). The sediment and dissolved nutrient plumes are located near the river mouth, whereas the low-salinity plume extends offshore over the shelf. Driven mainly by sediment loading and freshwater discharge in the upstream river, the sediment plume exhibits large temporal and spatial changes (Ge et al., 2015a, 2015b, 2018), so that the transition between suspended sediment/dissolved nutrient and low-salinity plumes varies significantly with time and in space. In this multi-plume estuarine system, the plankton dynamics are much complex, which are manifested through the fully nonlinear interaction of physical, biological and chemical processes under varying suspended sediment environment (May et al., 2003; Barbosa et al., 2009; Shi et al., 2017). Field campaigns with few sampling sites and over a short time coverage are unable to resolve the fine structures of physical and biogeochemical components, especially within the frontal zones. Some simplified numerical models were developed to simulate the phytoplankton growth and nutrient cycles in turbid estuaries (May et al., 2003; de Swart et al., 2009). These models, however, usually failed to resolve the short-term highly-varying temporal and spatial scales, which integrate to form the mid- and long-term variability of the pelagic planktonic ecosystem. Assessing the impact of sediment plume on the ecosystem in a high-turbidity estuarine environment requires an integrated three-dimensional numerical model capable of comprehensively capturing the interactions between sediment and biogeochemical processes, which was demonstrated by previous modeling studies in Great Lakes (Ji et al., 2002; Chen et al., 2004), but was scarce in estuaries. Since sediment resuspension in the high-turbidity estuaries is highly controlled by tidal currents regulating with winds and waves, the leading physical drivers, such as tides, waves and dominant estuarine and costal currents, must be integrated into the model.

In this study, we applied a fully physical and biogeochemical coupled model to examine the impact of sediment plume on the variability of nutrients and phytoplankton in the mega turbid and eutrophic Changjiang (Yangtze) Estuary and inner shelf of the East China Sea (ECS). One novelty of this study is to highlight the development of a realistic, comprehensive biogeochemical model system consisting of the interaction among surface waves, sediments, tides, coastal/oceanic currents over finer temporal and spatial scales. The other novelty lies in the exploration of ecosystem responses to high nutrient loading in a high-turbidity estuarine environment.

This paper is organized as follows. In Section 2, the study area and massive collection of observational data in the Changjiang Estuary and adjacent inner shelf of the ECS are introduced, following with the description of the coupled physical and biogeochemical model. In Section 3, the validation results of the model via observational data are presented. In Section 4, the effect of the sediment plume on the offshore nutrient and phytoplankton dynamics is evaluated. In Section 5, the dynamics controlling the physical-and-biogeochemical interaction in the Changjiang Estuary and inner shelf of ECS are discussed. Finally, in Section 6, major findings are summarized and conclusions are drawn.

2. Study area, data and model

2.1. Study area

The region of the Changjiang Estuary and inner shelf of the ECS is a typical estuarine-shelf coastal zone with a large input of freshwater and sediment from the upstream river (Fig. 1a). Over the period of 1950–2010, the annually-averaged freshwater volume entering this estuary was ~896 km^3, with a sediment load of ~390 Mt (CWRC, 2011). The freshwater discharge and sediment loading were measured at the Datong hydrological station locating ~620 km upstream from the ECS. This station is considered as a boundary site between the river and estuary. The freshwater discharge varies significantly with seasons. The average freshwater discharge is ~40 km^3/s in the wet season and ~13 km^3/s in the dry season (Luan et al., 2016). Mixing of freshwater with the oceanic water forms a low-salinity plume. This plume changes seasonally in terms of its spreading areas and pathway, flowing either into the ECS shelf during summer or further away along the Zhejiang coast during winter (Chen et al., 1994; Ge et al., 2015b). In summer, the large freshwater discharge makes the low-salinity plume enter the ESC shelf region, where it interacts with the large-scale regional oceanic circulations, such as the Yellow Sea Coastal Current (YSCC), the intrusion of Taiwan Warm Current (TWC, a sub-stream of the Kuroshio Current) and even Kuroshio (Chen et al., 1994, 2008) (Fig. 1a).

The abundant sediment loading from the upstream Changjiang River makes this estuary and its adjacent inner shelf of the ECS become a high-turbidity environment. The high-turbidity are clearly appeared in remote sensing images and measured in the field surveys (Siswanto et al., 2011; Sokoletsky et al., 2014; Ge et al., 2015a, 2015b). The suspended sediment concentration varied significantly with time and in space, with a range of ~0.1–1.0 g/l near the surface inside the estuary and of < 0.2 g/l in the offshore region (Ge et al., 2015a, 2015b).

In the recent years, with the rapid economic growth and corresponding increase in fertilizer use in agriculture, the Changjiang Estuary has experienced a dramatic increase period in nutrient loading. The environmental monitoring recorded at the Datong station from 1960 to 2000 indicated a sharp rise in nutrients, with the concentration of dissolved inorganic nitrogen (DIN) and phosphate (DIP) increasing from ~20 μmol/l to ~130 μmol/l, and from ~0.2 μmol/l to ~1.6 μmol/l, respectively (Li et al., 2007). This evidence was also reported early by Chen et al. (2003b) based on other data sources. In contrary to DIN and DIP, however, the dissolved inorganic silicate (DSi) dropped from ~120 μmol/l to ~70 μmol/l, resulting from fixation of DSi within hundreds of reservoirs built along the Changjiang river (Friedl and Wüest, 2002). These nutrient changes have caused severe eutrophication problems in the area and a dramatic change in the ratio of N: Si in the Changjiang Estuary and inner shelf (Zhou et al., 2008; Jiang et al., 2010; Zhu et al., 2014; Zhou et al., 2017).

Under a nutrient-rich environment, the high primary production and phytoplankton bloom were often observed in the Changjiang Estuary and it adjacent inner shelf of the ECS (Furuya et al., 1996, 2003), with a Chlorophyll-*a* (Chl-*a*) concentration of > 10 μg/l off the (Chen et al., 2003b; Zhu et al., 2009) and even reached ~20 μg/l when the harmful algal bloom occurred (Chen et al., 2003b). The diatom remains to be a predominant species contributing to the total phytoplankton Chl-*a* ($> 90\%$). Recent surveys reported that dinoflagellates have become dominant component in the phytoplankton community, particularly in the high resuspended sediment plume (Chen et al., 2003b) and in eutrophic onshore waters influenced by the low-salinity plume (Jiang et al., 2015).

2.2. The cruise data

Massive physical and biogeochemical data were collected from multiple field campaigns. Observational sites covered the river channel, estuary and inner shelf of the ECS (Fig. 1b). Responding to different patterns of Changjiang River plume's extensions in summer and winter around the inner shelf, 14 more sampling sites were placed in the south of the Changjiang Estuary during winter plus additional 12 sites in the east of the inner shelf in summer (Fig. 1b). A total of 90 and 92 sites were visited during the summer and winter cruises, respectively. Physical and biogeochemical variables were measured at these sites. The physical variables contained water velocities from a vessel-mounted Acoustic Doppler Current Profiler (ADCP), temperature and salinity

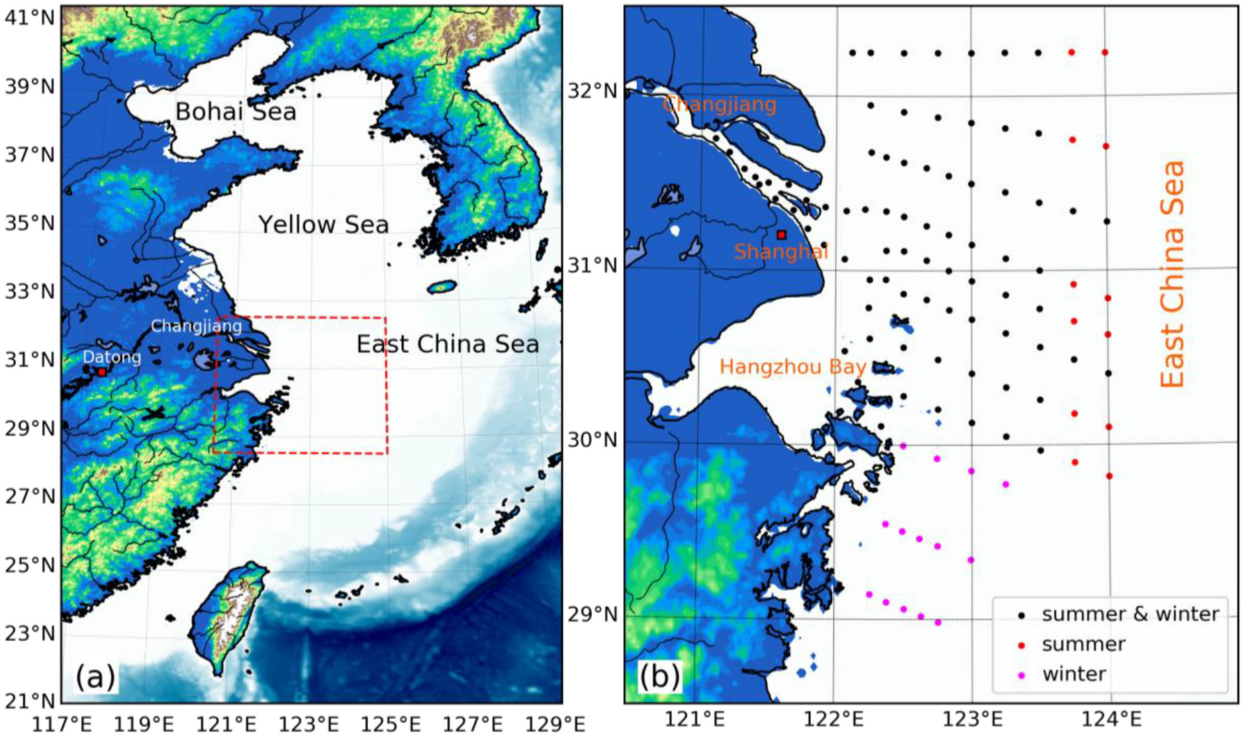

Fig. 1. The locations of the Changjiang River, the Datong hydrological station and the East China Sea (a). The panel (b) is an enlarged view of the area bounded by the dashed rectangle in panel (a). The pink and red dots indicate the survey sites taken in winter and summer, respectively. The black dots indicate the survey sites taken in both winter and summer. (For interpretation of the references to color in this figure legend, the reader is referred to the web version of this article.)

from sensors of Conductivity-Temperature-Depth (CTD). The biogeochemical variables included pH, nutrients including DIN, DIP, ammonia (NH4), and DSi, Chl-*a*, and suspended particulate matter (SPM). Cruises periods covered every winter and summer over the period of 2015 to 2017.

2.3. The satellite data

Both surface sediment concentration and phytoplankton Chl-*a* can be calculated from satellite remote sensing data (O'Reilly et al., 1998; Shen et al., 2010). In this study the satellite data were used for model validation and interpretation. The data came from two sources. One was the 4-km-resolution-mapped daily Chl-*a* field from Moderate Resolution Imaging Spectroradiometer Aqua satellite (MODIS-Aqua, https://oceancolor.gsfc.nasa.gov/data/aqua/), which covered the period from January 1, 2005 to December 31, 2016. The other one was the 500-m-resolution-mapped hourly sky-view observational data from the Multi-channel Geostationary Ocean Color Imager (GOCI) satellite, which covered the East Asian seas and recorded every 8 h per day (Choi et al., 2012, 2014). Surface Chl-*a* concentrations were retrieved and calculated using the ocean chlorophyll 2 algorithm (OC2) (O'Reilly et al., 1998; Ryu et al., 2012) through the GOCI Data Processing System (GDPS version 1.4.1) from 2012 to 2016, in which the Korea Ocean Satellite Center (KOSC) standard was applied in atmospheric correction. For public access, the daily product contained three snapshots taking at 10:30 am, 11:30 am and 12:30 am, respectively.

Generally, in coastal optically complex waters, Chl-*a* algorithms suffer from the contamination by colored particulate and dissolved substances. Using the semi-empirical radiative transfer (SERT) algorithm with physical based empirical coefficients (Shen et al., 2010), the GOCI optical reflectance data were used to estimate surface sediment concentrations in the Changjiang Estuary (Choi et al., 2012; He et al., 2013; Ge et al., 2015b), as well as Chl-*a* (Choi et al., 2014; Piwowarczyk et al., 2016; Sun et al., 2018). Previous studies have already confirmed the reliability of GOCI production for the Chl-*a* under the interference of colored dissolved organic matters (Lamquin et al., 2012; Hu et al., 2012).

2.4. Hydrodynamic model

Main hydrodynamic forcings and components in the Changjiang Estuary include the astronomical tide, river discharge, wind, waves, coastal/oceanic currents, and the sediment. The core system of the physical numerical model is the Finite-Volume Community Ocean Model (FVCOM). FVCOM is an unstructured-grid community ocean model, in which governed equations were discretized and solved using the finite-volume integration algorithm (Chen et al., 2003a) and gradually upgraded to include multiple hydrodynamic and ecosystem modules (Chen et al., 2013). The non-overlapping triangular grid configured in FVCOM provided accurate geometrical fitting for irregular coastlines while guaranteeing flexibility for refining the grid in steep bathymetry, islands, or regions of interest (Chen et al., 2003a; Chen et al., 2006; Qi et al., 2018). An accurate finite-volume second-order Ruge-Kutta algorithm guaranteed volume and mass conservations of the momentum fluxes over each iteration. Horizontal diffusion was parameterized based on Smagorinsky's formation (Smagorinsky, 1963) and vertical turbulent mixing was calculated using the 2.5-level Mellor and Yamada turbulence model (Chen et al., 2013).

FVCOM is a fully current-wave coupled model (Chen et al., 2013). An unstructured-grid version of the surface wave model-SWAN was developed on the platform of FVCOM and named “FVCOM-SWAVE” (Qi et al., 2009). The FVCOM-SWAVE implemented to FVCOM as a wave module and coupled with hydrodynamic component of FVCOM. This coupled model been applied for the coastal wave and inundation applications with inclusion of wave-current interactions (Wu et al., 2011a; Ge et al., 2013; Beardsley et al., 2013; Chen et al., 2013; Qi et al., 2018).

FVCOM also has incorporated a sediment module, covering from suspended sediment, to bed-load transport and layered bed-soil dynamics (Chen et al., 2006). This model has the ability of supporting

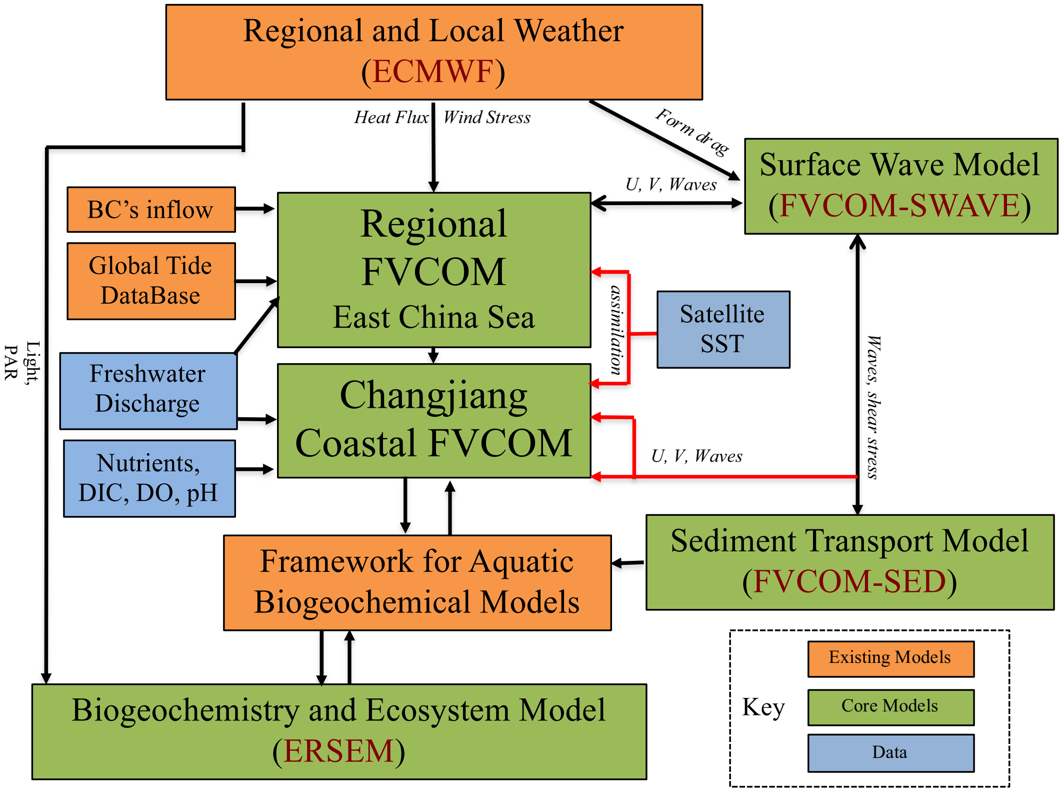

Fig. 2. Framework of the FVCOM-based coupling model system for physical and biogeochemical dynamics, including regional FVCOM model for the East China Sea and adjacent seas, coastal-estuarine FVCOM model for the Changjiang Estuary, the surface wave model FVCOM-SWAVE, sediment model FVCOM-SED, the biogeochemistry and ecosystem model FVCOM-ERSEM.

unlimited sediment classes for non-cohesive and cohesive sediment dynamics. Additionally, the wave and sediment have been fully coupled with the hydrodynamic kernel with their physical interactions (Wu et al., 2011a; Ge et al., 2018). The two-way coupling was considered in this modeling. This means individual process (such as waves) can impact on the other two processes (e.g. current and sediment).

2.5. Biogeochemical model

The biogeochemistry and ecosystem dynamics are simulated by the European Regional Seas Ecosystem Model (ERSEM ver. 15.06), which is a generic and well established lower-trophic level marine food web and biogeochemical cycling model (Butenschon et al., 2016). It resolves the ecosystem dynamics with nutrients and carbon cycles in the low trophic levels. It divides the phytoplankton, zooplankton and benthos into function groups, and calculates the biomass for the group individually. The model calculates various state variables, including pelagic and benthic living organisms, dissolved and particulate nutrients, dissolved oxygen and carbonates. ERSEM considers the functional groups following the lower trophic food-web chain from primary producers of phytoplankton, consumers like zooplankton, to decomposers of bacteria. For phytoplankton, ERSEM could consider up to four types, according their group sizes. They include pico-, nano-, and microphytoplankton, and diatoms. ERSEM accounts for up to three types of zooplanktons in the system, from meso-, and microzooplankton and heterotrophic nanoflagellates. For decomposers, only one type of heterotrophic bacteria is considered. Chl-*a* is determined separately in the model based on the quantification formulation (Geider et al., 1997). ERSEM is also equipped with a comprehensive benthic model (Ebenhoh et al., 1995) and a fully resolved carbonate system. It provides active nutrients and mass exchanges in the water-sediment interface. The ERSEM considers both dissolved and particulate organic matter, including labile dissolved organic matter, semi-labile organic matter, semi-refractory organic matter, small particulate organic matter, medium size particulate organic matter, large particulate organic matter. The particulate organic matter for nitrogen, phosphate and silicate are all considered in autochthonous compounds, but not external/forced fluxes (Butenschon et al., 2016). All the biogeochemical representation and mathematical formulations in ERSEM were described in detail in Butenschon et al. (2016).

3. Coupling of physical and biogeochemical models

3.1. Physical-biogeochemical model coupling

Coupling between FVCOM and ERSEM were utilized through FABM (Framework for Aquatic Biogeochemical Models; http://fabm.net) (Bruggeman and Bolding, 2014). The aim of this coupling is to provide FVCOM with a mechanism to easily incorporate new and existing biogeochemical models: FABM is a domain-independent programming framework with support for any number of processes, prognostic variables, diagnostic variables, and advanced features such as surface- and bottom layers (sea ice biota, benthos, sediment) and multiple feedbacks to physics. It comes with a comprehensive library of existing biogeochemical models, including descriptions of suspended sediment, redox chemistry (BROM) and pelagic and benthic ecosystems (NPZD, ERGOM, ERSEM).

FABM runs as part of its "host model", in this case, it is FVCOM. In a coupled FVCOM-FABM simulation, the ERSEM can be run either offline or online simultaneously with FVCOM with variable exchanges through FVCOM-FABM coupler (Bruggeman and Bolding, 2014). FABM itself provides information to biogeochemical processes, including source terms and residual vertical velocities (e.g., sinking rates) of prognostic variables, and the value of diagnostics. It doesn't handle features related to hydrodynamics or the spatial domain, e.g., transport of biogeochemical variables, surface boundary conditions (dilution/

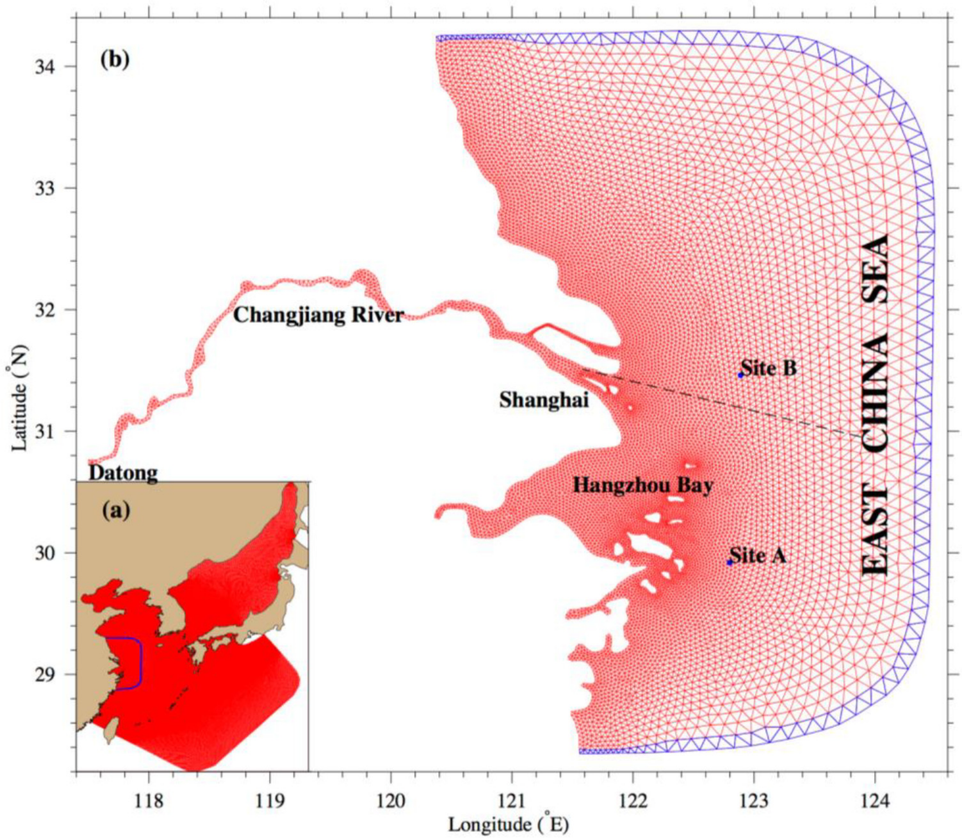

Fig. 3. Unstructured meshes for the shelf-scale East China Sea model (a) and coastal-estuarine scale Changjiang Estuary model (b). Two individual locations (Site A and B) and one section (blue dashed line) from the river mouth to the offshore region are included in (b). (For interpretation of the references to color in this figure legend, the reader is referred to the web version of this article.)

concentration due to precipitation/evaporation, open boundary conditions), rivers, reading restart files, and saving output. It also doesn't manage the memory for spatially explicit fields, e.g., the physical environment and the biogeochemical variables themselves. All these features are implemented in the FVCOM-FABM coupler.

Additionally, a python-based open-source utility PyFVCOM is used to easily manipulate and analyze the results from FVCOM-FABM-ERSEM simulation (Cazenave and Bedington, 2018).

3.2. *Integration of model system and configuration*

The model system for the Changjiang Estuary (Fig. 2) consisted of a shelf-scale East China Sea model and coastal-estuarine scale model for the Changjiang Estuary that incorporated waves and sediment dynamics. Wave-current-sediment interactions were activated only in the coastal-estuarine scale model, and coupling approach was extensively described in Ge et al. (2013). Differing from Ge et al. (2013), the upgraded version included the coupling of ERSEM.

The model grids for the regional and coastal domains were shown in Fig. 3. The regional model covers the adjacent shelf seas, including the Bohai Sea, Yellow Sea and the East China Sea (Fig. 4a), with a mesh resolution of ~3 km along the coastal region and Kuroshio path and meandering region (Chen et al., 2008; Ge et al., 2013). The large domain provides the boundary conditions of tide, ocean circulation and waves to the higher resolution coastal domain.

The coastal-estuarine domain for the Changjiang Estuary was discretized as the refined mesh with a resolution of ~1–3 km in the river mouth and coastal region (Fig. 3b). The upstream river boundary extended to the Datong station, which was the closest hydrological station to the tidal-limit measuring runoff rate, sediment flux and biological variables' concentrations. The coastal-estuarine domain covered the high-turbidity region in the estuary, including the Hangzhou Bay and the Jiangsu offshore region. The lateral open boundary was placed at 124.5°E, while the north and south lateral boundaries were located at 34.2°N and 28.25°N, respectively, with the purpose of eliminating the noise from the boundaries in our estuarine region of interest.

The Connecting between the regional and coastal domains was performed with a one-way nesting method. These two model meshes shared a common-grid layer with identical bathymetry, horizontal and vertical coordinates (blue lines in Fig. 3). This common-grid nesting method guaranteed the conservation of mass and momentum during regional-to-coastal nesting (Chen et al., 2013; Ge et al., 2013; Qi et al., 2018), thus this coupling of physical and biogeochemical dynamics through FABM was only active in the coastal-estuarine scale domain (Fig. 2).

The simulation covered the period from January 1, 1999 to December 31, 2016. The atmospheric conditions were driven by ERA Interim data from European Centre for Medium-Range Weather Forecasts (ECMWF). Surface wind velocities at 10 m height, shortwave, longwave, latent and sensible radiation flux were provided at a 6-hour interval. Lateral boundary conditions were specified with a hybrid forcing of astronomical tide and subtidal oceanic currents. The tidal boundary condition for the regional domain includes eight major tide harmonic constituents, M_2, S_2, K_2, N_2, K_1, O_1, P_1, and Q_1, retrieved from TPXO 7.2 Global Tidal Solution (Egbert and Erofeeva, 2002). Volume transport along the lateral boundary is interpolated from daily HYCOM/NCODA Global 1/12° Analysis data (GLBa0.08 branch). The upstream river boundary was driven by the daily freshwater and sediment discharges collected at the Datong station (www.cjh.com.cn).

Satellite-derived sea surface temperature (SST) data were assimilated in the model with a nudging algorithm (Chen et al., 2013). Daily SST data from the Advanced Very High-Resolution Radiometer (AVHRR) L4 at 0.25° resolution was assimilated in the model over the period from 1999 to 2004, while the data from GHRSST/JPL (https://podaac.jpl.nasa.gov/GHRSST) at 0.011° resolution over the period from 2005 to 2016. The wave model followed the configuration described in Ge et al. (2013). The sediment model shared the same parameters as Ge et al. (2015a, 2015b). The spatially non-uniform distribution of the

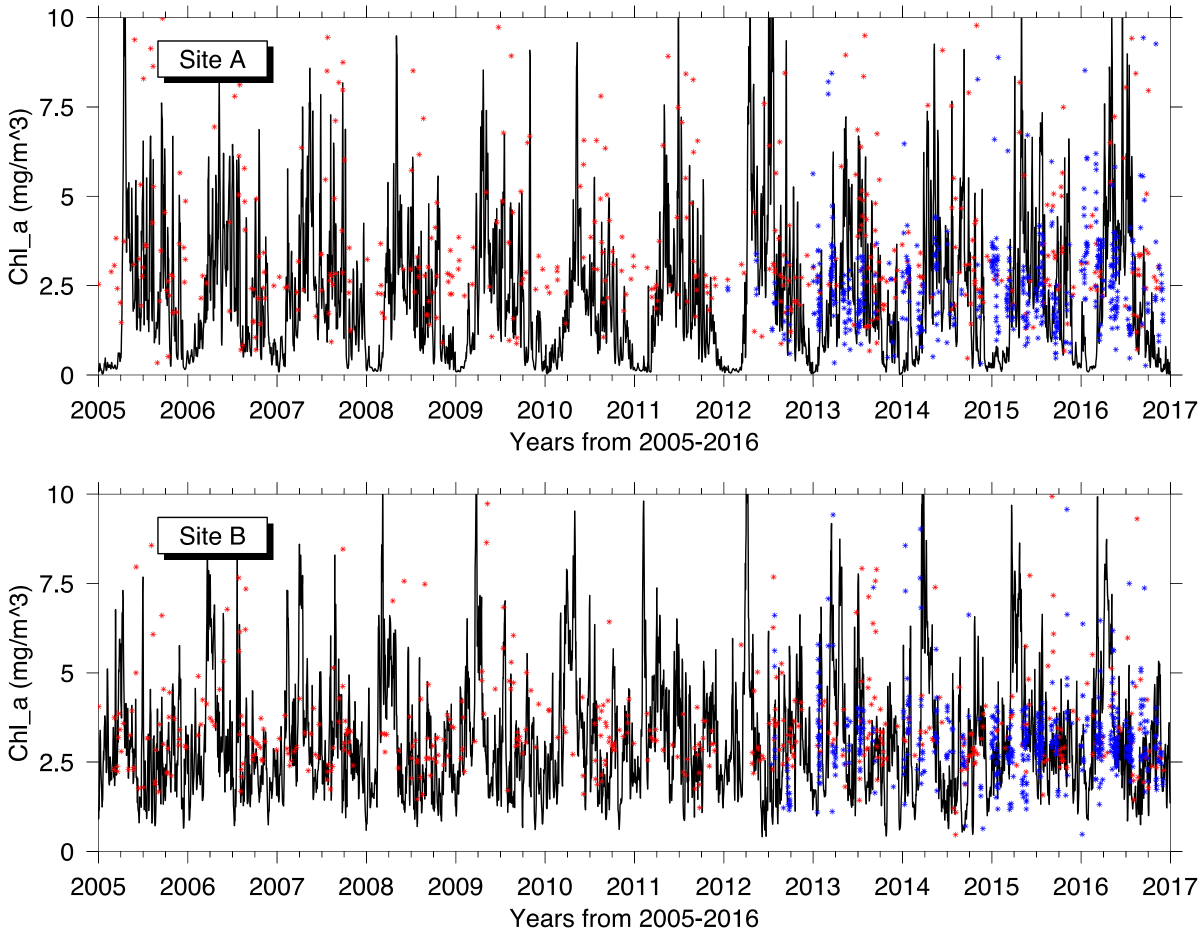

Fig. 4. Comparisons between model-simulated and satellite remote-sensing-derived surface Chl-*a* concentrations at Site A and Site B. The red and blue dots indicate the Chlorophyll-*a* concentration values from MODIS and GOCI satellites, respectively. (For interpretation of the references to color in this figure legend, the reader is referred to the web version of this article.)

critical shear stress for erosion, adopted from Ge et al. (2015a, 2015b), were also applied in this configuration.

Since the main purpose of our modeling study was to examine the nutrients and phytoplankton dynamics in the pelagic system and the benthic ecosystem is not a dominant contributor, only the pelagic (non-benthic) dynamics were considered here.

To avoid zero values of the carbonate system variables at the river nodes, the dissolved oxygen (DO), carbonate bio-alkalinity, total alkalinity, and carbonate total dissolved inorganic carbon (DIC) were specified by constant values of 300 mmol O/m^3, 2.50 μmol/kg, 2065.0 μmol/kg, and 2200.0 mmol C/m^3, respectively. Nutrient concentrations at the lateral boundaries were interpolated from the World Ocean Atlas 2013 ver. 2 (https://www.nodc.noaa.gov/OC5/woa13/). The carbonate system variables (DIC and total alkalinity) were determined from the Global Ocean Data Analysis Project version 2 (GLODAPv2, Olsen et al., 2016) and imposed as monthly climatology. The parameters and biogeochemical coefficients used in ERSEM simulation were listed in Table 1.

3.3. Univariate verification

To validate the model, the remote sensing data of Chl-*a* concentration from satellites (MODIS-Aqua and GOCI) were used to perform model-data comparisons. Two sites located offshore of the sediment plume were selected for this comparison (Fig. 3): site A (122.89°E, 31.46°N) and site B (122.80°E, 29.92°N). As shown in Fig. 4, the daily MODIS-Aqua Chl-*a* data for 2005–2016 (red dots) were combined with the GOCI Chl-*a* data for 2012–2016 (blue dots) and then used to verify the model-simulated Chl-*a* data (solid line). Two distinct blooms were evident from the observational Chl-*a* in spring and in autumn, respectively. These blooms were captured by the model-simulated results. The peaks of MODIS and simulated Chl-*a* concentrations both reached ~10 mg/m^3 during the spring bloom. The root-mean-square-error between them were 2.2 mg/m^3 and 2.47 mg/m^3 at Site A and B, respectively, indicating this coupled model system successfully reproduced the magnitude and seasonal variations of Chl-*a* in the offshore regions. Besides, the comparison between GOCI data and simulated Chl-*a* shown that short-term temporal variations could also be captured by the model simulation. Although the validation was conducted on a daily basis, it showed the variations over the time scale from seconds to minutes as the model was integrated for iteration.

3.4. Multivariate verification

In addition to useful independent and univariate assessments, the comparison between model-simulated results and observations for all common variables simultaneously provides a better evaluation of the overall performance of the model (Allen and Somerfield, 2009; Stow et al., 2009). To determine the model's capability of revealing the realistic dynamics in the offshore region, Principle Component Analysis (PCA) was applied to reduce the dimensionality of the dataset and to identify the significant underlying components (Allen and Somerfield, 2009). PCA was performed on both instantaneous observed values and daily averages of variables at measurement sites from surface to bottom

Table 1
Variable definitions and values used in FVCOM-ERSEM coupling.

Symbol	Definition	Value				Unit
pCO2a	Mole fraction of carbon dioxide in air	385				10^{-6}
a0w	Adsorption coefficient of clear water	0.015				$\mathrm{m^{-1}}$
b0w	Backscatter coefficient of clear water	0.00135				$\mathrm{m^{-2}}$
pEIR_eow	Photosynthetically active fraction of shortwave radiation	0.5				-1
EPSESSa	Specific shortwave absorption coefficient of silt	0.00004				$\mathrm{m^2\ mg^{-1}}$
EPSESSb	Specific shortwave backscatter coefficient of silt	0.00001				$\mathrm{m^2\ mg^{-1}}$
N1p	Initialization concentration of phosphate phosphorus	0.4				$\mathrm{mmol\ P\ m^{-3}}$
N3n	Initialization concentration of nitrate nitrogen	8				$\mathrm{mmol\ N\ m^{-3}}$
N4n	Initialization concentration of ammonium nitrogen	0.1				$\mathrm{mmol\ N\ m^{-3}}$
N5 s	Initialization concentration of silicate	4.5				$\mathrm{mmol\ Si\ m^{-3}}$
O2o	Initialization concentration of oxygen	300				$\mathrm{mmol\ O_2\ m^{-3}}$
O3c	Total dissolved inorganic carbon	2130				$\mathrm{mmol\ C\ m^{-3}}$
	Labile (R1), semi-labile (R2) and refractory (R3) dissolved organic carbon	R1	R2		R3	
c	Initialization carbon concentration	10	12		12	$\mathrm{mg\ C\ m^{-3}}$
n	Initialization nitrogen concentration	0.14	–		–	$\mathrm{mmol\ N\ m^{-3}}$
p	Initialization phosphorus concentration	0.01	–		–	$\mathrm{mmol\ P\ m^{-3}}$
	Small (R4), medium (R6) and large (R8) particulate organic carbon	R4	R6		R8	
iopABS	Specific shortwave absorption	0.00001	0.00001		0.00001	$\mathrm{m^2\ m^{-1}C}$
iopBBS	Specific shortwave backscatter	0.000016	0.000016		0.000016	$\mathrm{m^2\ m^{-1}C}$
rm	Sinking velocity	1	5		10	$\mathrm{m\ d^{-1}}$
c	Initialization carbon concentration	7.2	17		0.17	$\mathrm{mg\ C\ m^{-3}}$
n	Initialization nitrogen concentration	0.1	0.24		0.0024	$\mathrm{mmol\ N\ m^{-3}}$
p	Initialization phosphorus concentration	0.007	0.02		0.0002	$\mathrm{mmol\ P\ m^{-3}}$
s	Initialization silicate concentration	–	0.1		0.001	
	benthic dissolved (Q1), particulate (Q6) organic, refractory (Q7) matter	Q1	Q6		Q7	
remin	Remineralisation rate	0.1	0.05		0.01	$\mathrm{d^{-1}}$
pN3	Nitrate fraction of remineralised nitrogen (remainder is ammonium)	0.9	0.9		0.9	Dimensionless
c	Initialization carbon concentration	18.9	3052		30,520	$\mathrm{mg\ C\ m^{-2}}$
n	Initialization nitrogen concentration	0.6	3.5		80	$\mathrm{mg\ N\ m^{-2}}$
p	Initialization phosphorus concentration	0.0035	0.5		8	$\mathrm{mg\ P\ m^{-2}}$
resuspension	Enable resuspension	True	–		–	Dimensionless
vel_crit	critical shear velocity for resuspension	0.2	–		–	m/ s
s	initialization silicate concentration	149	–		–	$\mathrm{mg\ Si\ m^{-2}}$
pel_nitq10	q_{10} temperature coefficient of pelagic nitrification	2				Dimensionless
pel_nitISWph	ph impact on pelagic nitrification (0:off,1:on)	1				Dimensionless
pel_nitsN4N3	Specific nitrification rate of pelagic nitrification	0.5				$\mathrm{1\ d^{-1}}$
pel_nitchN3o	Michaelis-Menten constant for cubic oxygen dependence of pelagic nitrification	2700				$\mathrm{(mmol\ O2\ m^{-3})^3}$
pel_nitchN4n	Michaelis-Menten constant for cubic ammonium dependence of pelagic nitrification	0.5				$\mathrm{(mmol\ N\ m^{-3})^3}$
Ref_temp	Reference temperature	10				degree C
	Diatoms (P1), Nanoflagellates (P2), Picoplankton (P3), and dinoflagellates (P4) phytoplankton functional groups	P1	P2	P3	P4	
sum	Maximum specific productivity at reference temperature	1.375	1.625	2	1.125	$\mathrm{1\ d^{-1}}$
q10	q10 temperature coefficient	2	2	2	2	Dimensionless
srs	Specific rest respiration at reference temperature	0.04	0.04	0.045	0.035	$\mathrm{1\ d^{-1}}$
pu_ea	Excreted fraction of phytoplankton's primary production	0.2	0.2	0.2	0.2	Dimensionless
pu_ra	Respired fraction of phytoplankton's primary production	0.2	0.2	0.2	0.2	Dimensionless
qnlc	Minimum nitrogen to carbon ratio	0.0042	0.005	0.006	0.0042	$\mathrm{mmol\ N\ mg^{-1}C}$
qplc	Minimum phosphorus to carbon ratio	0.0001	0.000225	0.00035	0.0001	$\mathrm{mmol\ P\ mg^{-1}C}$
xqcp	Threshold for phosphorus limitation (relative to redfield ratio)	1	1	1	1	Dimensionless
xqcn	Threshold for nitrogen limitation (relative to redfield ratio)	1	1	1	1	Dimensionless
xqp	Maximum phosphorus to carbon ratio (relative to redfield ratio)	2	2	1.5	2.7	Dimensionless
xqn	Maximum nitrogen to carbon ratio (relative to redfield ratio)	1.075	1.075	1.05	1.1	Dimensionless
qun3	Nitrate affinity	0.0025	0.004	0.006	0.002	$\mathrm{(m^3\ mg^{-1}C)d^{-1}}$
qun4	Ammonium affinity	0.0025	0.004	0.007	0.002	$\mathrm{(m^3\ mg^{-1}C)d^{-1}}$
qurp	Phosphate affinity	0.003	0.004	0.006	0.002	$\mathrm{(m^3\ mg^{-1}C)d^{-1}}$
snplux	Specific tendency of luxury uptake of nutrients towards maximum quota	1	1	1	1	$\mathrm{1d^{-1}}$
use_Si	If phytoplankton use silicate	True	False	False	False	Dimensionless
qsc	Maximum silicate to carbon ratio	0.0118	–	–	–	$\mathrm{mmol\ Si\ mg^{-1}C}$
chs	Michaelis-Menten constant for silicate limitation	0.2	–	–	–	$\mathrm{mmol\ m^{-3}}$
sdo	1.1 of minimal specific lysis rate	0.05	0.05	0.055	0.045	$\mathrm{1\ d^{-1}}$
alpha	Initial slope of pi-curve	4	5	6	3	$\mathrm{((mg\ C\ m^2\ mg^{-1}\ Chl)\ W^{-1})d^{-1}}$
beta	Photoinhibition parameter	0.07	0.1	0.12	0.06	$\mathrm{((mg\ C\ m^2\ mg^{-1}\ Chl)\ W^{-1})d^{-1}}$
phim	Maximum effective chlorophyll to carbon photosynthesis ratio	0.06	0.025	0.015	0.045	$\mathrm{mg\ Chl\ mg^{-1}C}$
uB1c_O2	Oxygen produced per unit of carbon fixed	0.11	0.11	0.11	0.11	$\mathrm{mmol\ O_2\ mg^{-1}C}$
urB1_O2	Oxygen consumed per unit of carbon respired	0.1	0.1	0.1	0.1	$\mathrm{mmol\ O_2\ mg^{-1C}}$
iopABS	Specific shortwave absorption	0.007	0.0041	0.023	0.008	$\mathrm{m^2\ mg^{-1}\ Chl}$
iopBBS	Specific shortwave backscatter	0.00048	0.003	0.003	0.00048	$\mathrm{m^2\ mg^{-1}\ Chl}$
resm	Maximum nutrient-limitation-induced sinking velocity	5	0	0	5	$\mathrm{m\ d^{-1}}$
c	Initialization carbon concentration	8	5.9	5.9	5.9	$\mathrm{mg\ C\ m^{-3}}$
n	Initialization nitrogen concentration	0.1114	0.0926	0.0926	0.0926	$\mathrm{mmol\ N\ m^{-3}}$
p	Initialization phosphorus concentration	0.009	0.0036	0.0036	0.0036	$\mathrm{mmol\ P\ m^{-3}}$

(*continued on next page*)

Table 1 (*continued*)

Symbol	Definition	Value				Unit
Chl	Initialization chlorophyll *a* concentration	0.4	0.3	0.3	0.3	mg m^{-3}
P1s	Initialization silicate concentration of diatoms	0.128				mmol Si m^{-3}
P2calcify	Calcify of nanophytoplankton	TRUE				Dimensionless
L2sedL2	Sinking velocity of calcite	10				m d^{-1}
L2c0	Initialization carbon concentration of calcite	0.05				mg C m^{-3}
bL2remin	Remineralisation rate of benthic calcite	0.05				1 d^{-1}
bL2c	Initialization carbon concentration of benthic calcite	0.05				mg C m^{-2}
Mesozooplankton (Z4), microzooplankton (Z5), nanoflagellates (Z6)		Z4	Z5	Z6		
q10	Q10 temperature coefficient	2	2	2		Dimensionless
minfood	Michaelis-Menten constant to perceive food	12	12	12		mg C m^{-3}
chuc	Michaelis-Menten constant for food uptake	36	32	28		mg C m^{-3}
sum	Maximum specific uptake at reference temperature	1	1.25	1.5		1 d^{-1}
pu	Assimilation efficiency	0.6	0.5	0.4		Dimensionless
pu_ea	Fraction of unassimilated prey that is excreted (not respired)	0.5	0.5	0.5		Dimensionless
pe_R1	Dissolved fraction of excreted/dying matter	0.5	0.5	0.5		Dimensionless
srs	Specific rest respiration at reference temperature	0.015	0.02	0.025		1 d^{-1}
sd	Basal mortality	0.05	0.05	0.05		1 d^{-1}
sdo	Maximum mortality due to oxygen limitation	0.2	0.25	0.3		1 d^{-1}
chro	Michaelis-Menten constant for oxygen limitation	7.81	7.81	7.81		Dimensionless
qpc	Phosphorus to carbon ratio	0.000786	0.001	0.001		mmol P mg^{-1}C
qnc	Nitrogen to carbon ratio	0.0126	0.0167	0.0167		mmol N mg^{-1C}
R1R2	Labile fraction of produced dissolved organic carbon	1	1	1		1 d^{-1}
xR1p	Transfer of phosphorus to DOM, relative to POM	1.2	1.2	1.2		Dimensionless
xR1n	Transfer of nitrogen to DOM, relative to POM	1	1	1		Dimensionless
urB1_O2	Oxygen consumed per carbon respired	0.1	0.1	0.1		mmol O_2 mg^{-1}C
gutdiss	fraction of prey calcite that dissolves after ingestion	0.5	0.5	0.5		Dimensionless
c0	Background carbon concentration	0.0033	0.0033	0.0033		mg C m^{-3}
c	Initialization carbon concentration	1.2	7.2	2.421		mg C m^{-3}
Z4pu_eaR	Fraction of unassimilated detritus that is excreted (not respired)	0.9				Dimensionless
Z4Minprey	Food threshold for overwintering state of mesozooplankton	300				mg C m^{-2}
Z4repw	Specific overwintering respiration of mesozooplankton	0.0025				1 d^{-1}
Z4mort	Specific overwintering mortality of mesozooplankton	0.0025				1 d^{-1}
stempp	Specific excretion rate of excess phosphorus		0.5	0.5		1 d^{-1}
stempn	Specific excretion rate of excess nitrogen		0.5	0.5		1 d^{-1}
n	Initialization nitrogen concentration		0.12	0.0505		mmol N m^{-3}
p	Initialization phosphorus concentration		0.0113	0.047		mmol P m^{-3}
Bacteria		B1				
iswBlim	Nutrient limitation of bacteria (1:minimum of inorganic and organic availability,2:additive availability)	2				Dimensionless
q10	Q_{10} temperature coefficient of bacteria	2				Dimensionless
chdo	Michaelis-Menten constant for oxygen limitation of bacteria	0.31				Dimensionless
chn	Michaelis-Menten constant for nitrate limitation of bacteria	0.5				mmol N m^{-3}
chp	Michaelis-Menten constant for phosphate limitation of bacteria	0.1				mmol P m^{-3}
sd	Specific mortality of bacteria at reference temperature	0.05				1 d^{-1}
sum	Maximum specific uptake of bacteria at reference temperature	2.2				1 d^{-1}
pu	Efficiency of bacteria at high oxygen levels	0.6				Dimensionless
puo	Efficiency of bacteria at low oxygen levels	0.2				Dimensionless
srs	Specific rest respiration of bacteria at reference temperature	0.1				Dimensionless
sR1	Maximum turn-over rate of DOM of bacteria	1				1 d^{-1}
qpc	Maximum phosphorus to carbon ratio of bacteria	0.0019				mmol P mg^{-1}C
qnc	Maximum nitrogen to carbon ratio of bacteria	0.0167				mmol N mg^{-1}C
ur_o2	Oxygen consumed per carbon respired of bacteria	0.1				mmol O_2 mg^{-1}C
sR1N1	Mineralisation rate of labile dissolved organic phosphorus of bacteria	0				1 d^{-1}
sR1N4	Mineralisation rate of labile dissolved organic nitrogen of bacteria	0				1 d^{-1}
fsink	Scavenging rate for iron of bacteria	0.00007				1 d^{-1}
c0	Background carbon concentration of bacteria	0.01				mg C m^{-3}
rR2	Fraction of semi-labile DOC available to bacteria	0.0075				Dimensionless
rR3	Fraction of semi-refractory DOC available to bacteria	0.0025				Dimensionless
frR3	Fraction of activity respiration converted to semi-refractory DOC	0.3				Dimensionless
c	Initialization carbon concentration of bacteria	15.7				mg C m^{-3}
n	Initialization nitrogen concentration of bacteria	0.26				mmol N m^{-3}
p	Initialization phosphorus concentration of bacteria	0.029				mmol P m^{-3}

layers for salinity, temperature, Chl-*a*, SiO_3, NO_3, PO_4, SPM, NH_4, and pH.

Both cumulative proportion of the first three eigenvectors of observed and simulated variables were > 90%, and the first two eigenvectors aggregated > 85% (Table 2). This meant that the first principal component (PC1) and second principal component (PC2) were able to reproduce the main factors that described the variability of the system as captured in the observed variables. PC1 of observed and simulated variability accounted for 64.8% and 62.5%, respectively, both observed and simulated results indicated the very similar contribution of salinity, temperature, SiO_3, NO_3 and PO_4. PC2 was 22.8% and 23.4%, respectively, with the temperature to be the most essential. PC3 of the observed variability was mainly controlled by the combination of NH_4 and suspended sediment, while that of model simulated variability was under the mixed effect of NH4 and Chl-*a*.

The ordination values in the PCA demonstrated the similarity between the main modes of variability in both observed and modeled variables, and the seasonal changes associated with the controls on the

Table 2
PCA Analysis of the modeling and measuring variables.

Eigenvector	Observation			Simulation		
	PC1	PC2	PC3	PC1	PC2	PC3
pH	−0.039	0.054	0.149	−0.361	−0.067	0.016
NH_4	−0.021	−0.070	0.891	−0.202	0.142	0.502
PO_4	0.402	−0.227	−0.046	0.273	−0.384	−0.231
NO_3	0.446	0.017	0.012	0.470	0.109	0.152
SiO_3	0.543	0.048	−0.093	0.462	0.148	0.139
Chl-*a*	0.006	0.149	0.058	−0.159	0.125	0.687
Salinity	−0.581	−0.167	−0.116	−0.495	−0.283	−0.159
Temperature	−0.035	0.935	0.070	−0.153	0.835	−0.391
SPM	0.059	−0.116	0.389	0.160	−0.020	0.039
Variance	0.65	0.23	0.04	0.62	0.23	0.07
Variance%	64.89	22.84	3.75	62.49	23.46	7.28
Cumulative%	64.89	87.73	91.48	62.49	85.94	93.23

pelagic ecosystem and environmental conditions (Fig. 5). The samples of the two datasets in summer were in the positive direction of PC2 axis and the samples in winter were in the negative direction of PC2 axis because of the dominating control of temperature in PC2. The observation PCA points had a more compact distribution than the simulated results. This implied that the model reproduced the observed variability to some degree. The high positive values on PC2 axis were possibly related with the overestimation of river temperature. In general, both patterns from PCA showed some similarities, indicating the model revealed the major modes of seasonal effects of the biogeochemical variables, at least on winter/summer seasons.

4. Nutrient and phytoplankton simulations

4.1. Chl-a and sediment front

To determine the seasonal variability of phytoplankton under the condition with sediments, we calculated the seasonal means of surface Chl-*a* overlapped with the sediment concentration (Fig. 6). Four seasons were defined as follow, March–May as spring, June–August as summer, September–November as autumn and December–February as winter. At this level of aggregation, the model results clearly showed two distinct zones separated by the waters with high-concentration suspended sediment and with high phytoplankton Chl-*a* concentration, respectively. The computational domain contained several significant high-turbidity zones, including the Changjiang Estuary, Hangzhou Bay and the coastal region off Jiangsu Province. The model also reproduced the seasonal variation of sediment dynamics in the offshore regions of the Changjiang Estuary and Jiangsu. The sediment front in the Changjiang Estuary was confined within 122.5°E during spring and summer (Fig. 6a–b), but extended to 123°E in autumn and winter (Fig. 6c–d). In the Jiangsu offshore region, there was a similar pattern, but with further offshore extension in autumn and winter, which reached ~124.3°E in winter.

However, the extension of this sediment front is not uniquely controlled by the remote horizontal sediment advection. Local resuspension dynamics in combination with vertical stratification were responsible for the behavior and extension of the sediment plume. In spring and summer, in the offshore region, under strong stratification condition, it was due to the off-shore extension of the low-salinity river plume (Wu et al., 2011a, 2011b; Ge et al., 2015a, 2015b). The advection of riverine derived SSC was the major driving force since the ambient concentrations were low. Surface heating in these two seasons also played an important role in intensifying stratification. This limited the upward vertical transport of sediment in the offshore region and led to low SSC in the upper water column. With sufficient nutrient supply, the increase in light availability in the surface layers under a low SSC condition made a more favor environment for the phytoplankton growth in the offshore region compared to the nearshore and estuarine region.

In autumn and winter, the physical conditions changed. Due to decreasing freshwater discharge and colder weather-induced surface cooling, the offshore destratification occurred. Vertical mixing increased the local resuspension of sediment throughout the water column (Luo et al., 2017), producing the high broad-scale sediment concentration at the surface (Fig. 6d). Under lower water temperature and light penetration, the phytoplankton growth in the offshore region

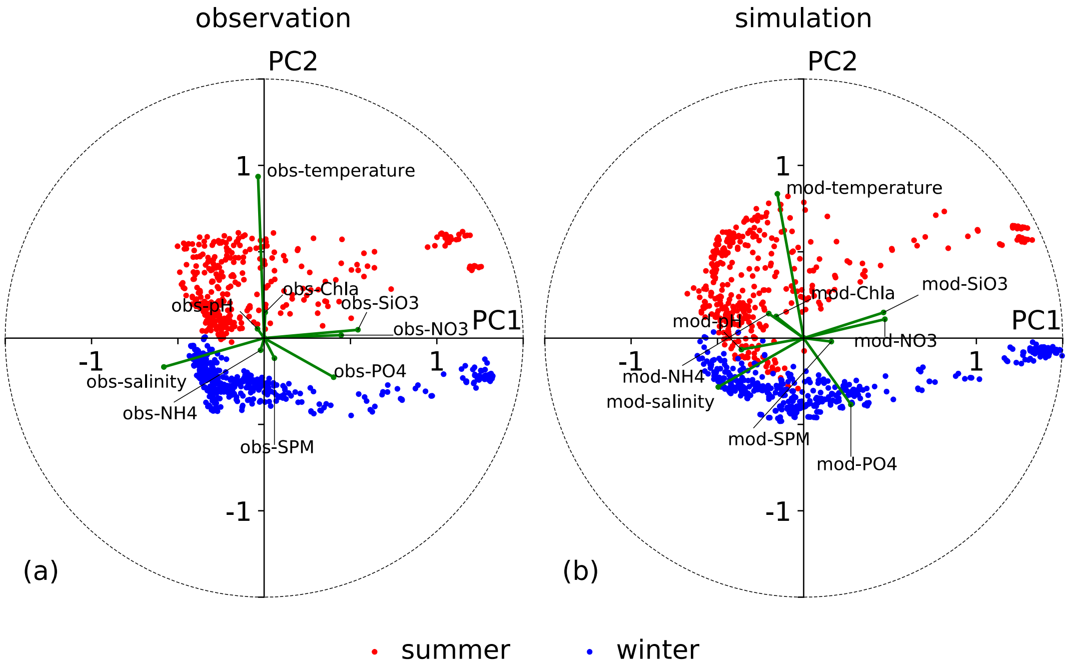

Fig. 5. Principle Component Analyses (PCA) based on observed (a) and simulated (b) Chl-*a*, nitrate, silicate, phosphate and ammonia concentrations as well as temperatures, salinities, pH levels and SPM values. The simulated values were the nearest equivalent to the measurements in temporal and spatial coordinates. Data were normalized before the analysis was performed. PC1 and PC2 indicate the first and second principal components, respectively.

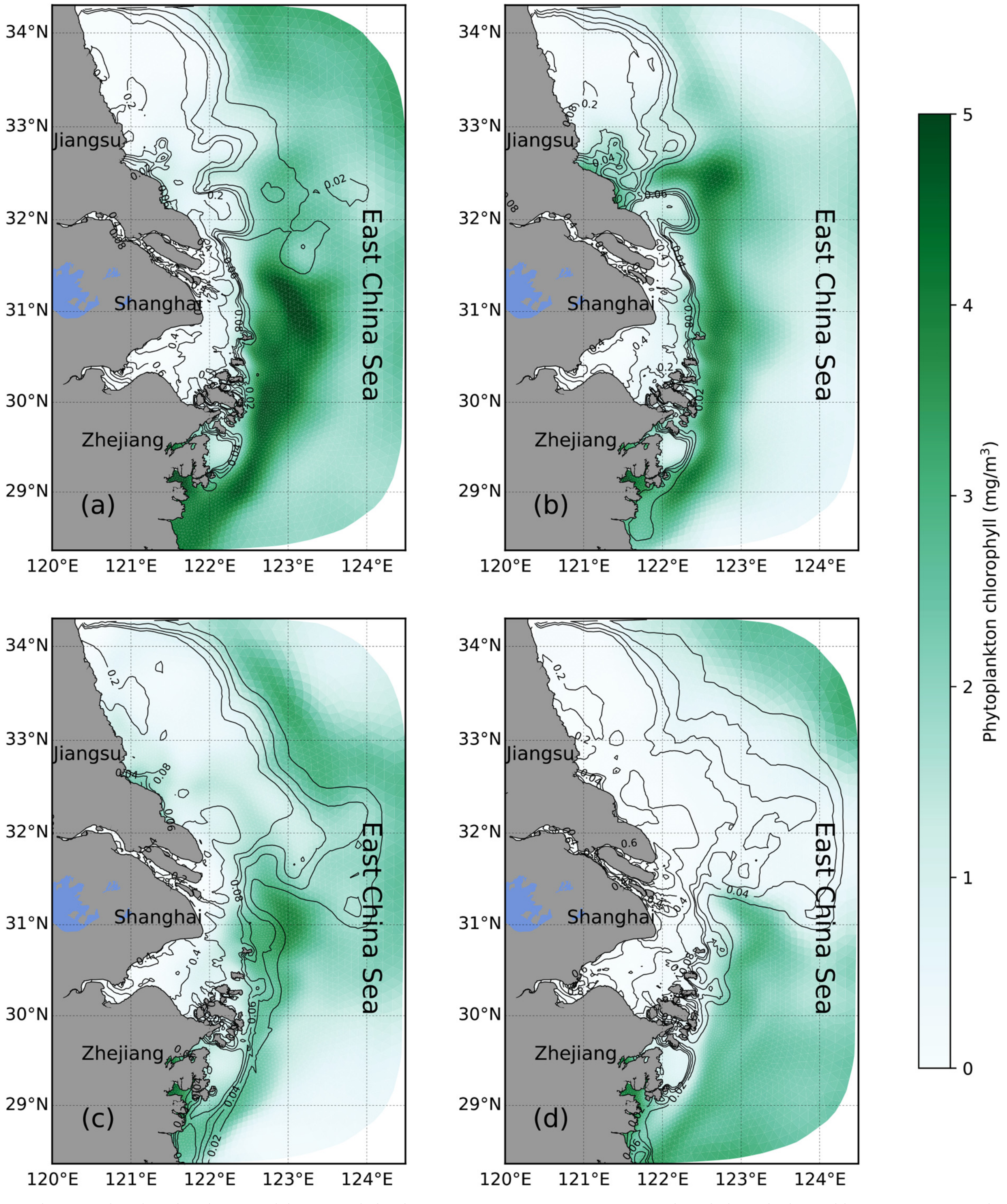

Fig. 6. Seasonal-averaged surface distributions of the suspended sediment concentration (contour, unit: g/l) and phytoplankton Chl-*a* concentration (colored image, unit: mg/m^3) during spring (a), summer (b), autumn (c) and winter (d). (For interpretation of the references to color in this figure legend, the reader is referred to the web version of this article.)

was greatly limited.

4.2. Diatom and non-diatom phytoplankton group

Multiple species of phytoplankton jointly contributed to the total Chl-*a* concentration in the observations and model results. In the shelf of the ECS, diatoms and dinoflagellates are the major groups and generally represent up to 90% of the total biomass in the spring bloom (Chen et al., 2003a, 2003b; Zhu et al., 2009). While the single specie *Skeletonema costatum* dominates the diatom group, dinoflagellates are represented by hundreds of species, covering sizes from microphytoplankton (> 20 μm), nanophytoplankton (2–20 μm), to picophytoplankton (< 2 μm). Nonetheless, the dominant specie is *Prorocentrum donghainese*. In order to facilitate the comparison with observations and known dynamics in the region, we have aggregated the model results for microphytoplankton, nanophytoplankton and picophytoplankton from FVCOM-ERSEM modeling results as a non-diatom phytoplankton group.

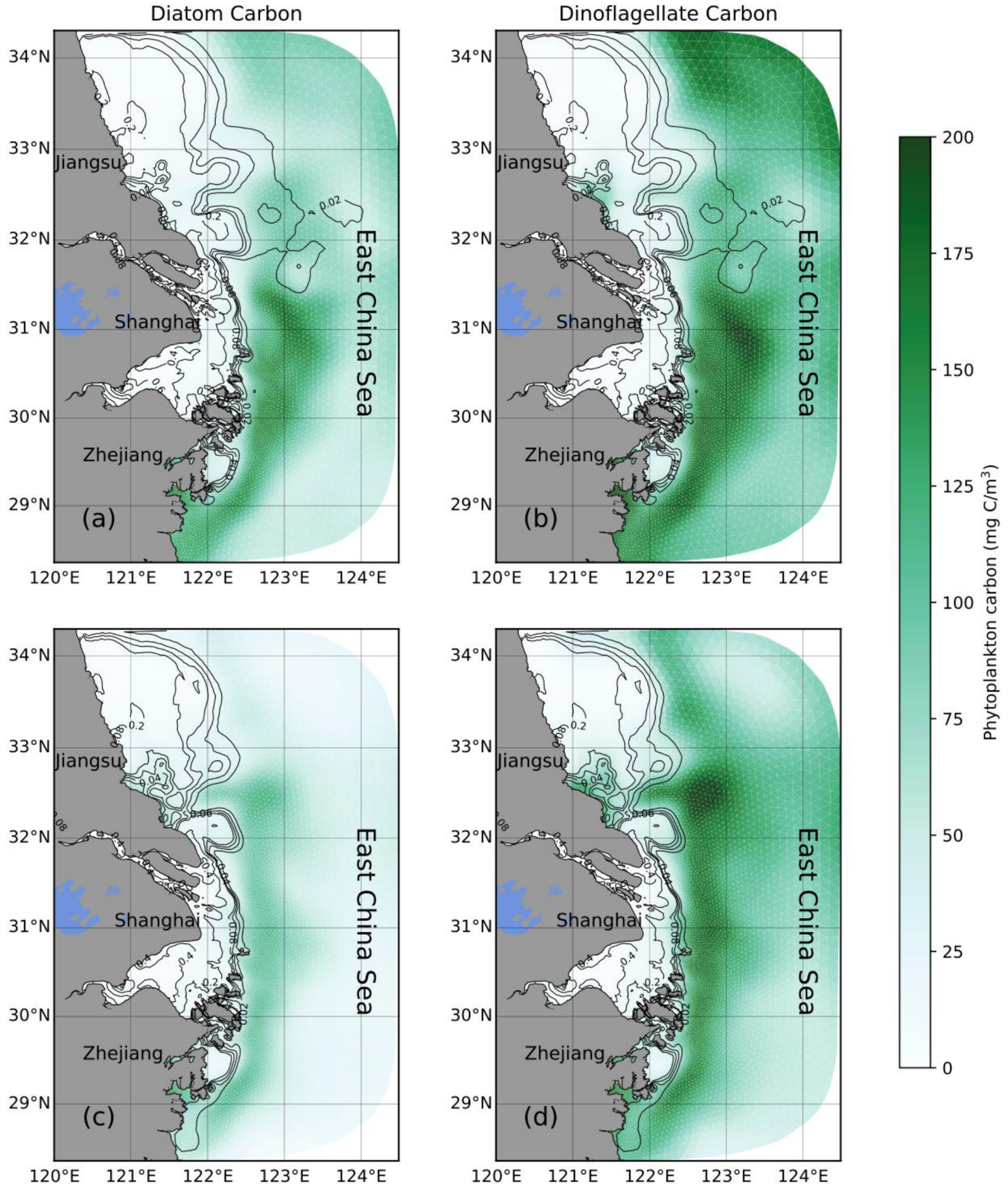

Fig. 7. Seasonal-averaged surface distributions of the suspended sediment concentration (unit: g/l) (contours) and biomass (colored image; unit: mg C/m^3) of diatom (a, c) and dinoflagellate (b, d) (colored image) during spring (a–b) and summer (c–d). (For interpretation of the references to color in this figure legend, the reader is referred to the web version of this article.)

To determine the major phytoplankton group that contributes to the increase of Chl-*a* in spring and summer (Fig. 6a–b), the surface carbon-based (not Chl-*a*-based) biomass of diatom and non-diatom phytoplankton were shown in Fig. 7. The overall diatom percentage in the phytoplankton community was about 43% during spring. The results showed that diatom carbon distribution (Fig. 7a) matched well with the pattern of the Chl-*a* concentration during spring season (Fig. 6a), indicating the diatom had a major contribution to the Chl-*a* concentration. However, the diatom biomass was weaker than the non-diatom group, including dinoflagellate and other small-size species. The distribution pattern of diatom followed the Chl-*a* distribution, which were confined offshore but closed to the sediment frontal boundary along the estuary, indicating light availability limits the diatom growth. Non-diatom biomass was higher offshore of the sediment front in the shelf region, particularly in the northeastern region, where the non-diatom concentration reached 200 mg C/m^3, while the Chl-*a* concentration remained low (50–75 mg C/m^3) in spring due to nutrient limitation.

In summer, the diatom percentage in total biomass of phytoplankton declined to 37%, especially on the offshore side of the sediment front (Fig. 7c). The wide diatom biomass regions shrank to a narrow band along the sediment front on the offshore side with a maximum concentration declining from ~175 to ~80 mg C/m^3, resulting from the diatoms' dependency on light and nutrient physiologically. On the other hand, non-diatom had high biomass both along the sediment front and even in the out region, with a maximum concentration of > 200 mg C/m^3 (Fig. 7d).

4.3. Dissolved nutrients

Taking the nitrogen flux from the Changjiang Estuary for example, the annual DIN flux was about 1.25 × 10^{11} mol yr^{-1}; the particulate nitrogen, however, was only about 0.9 × 10^{10} mol yr^{-1} (Gao et al., 2012). The content of PN was < 10% of total nitrogen. The particulate nutrient was only a small component in the whole nutrient based on the measurements in the Changjiang River (Gao et al., 2012). Among the various phosphorus forms, particulate phosphorus represented < 50%, and is closely related to the concentration of suspended sediment concentration (Liu et al., 2016). Nonetheless, the dissolved inorganic nutrients made the major contribution to the phytoplankton growth and ecosystem cycle. Therefore, the temporal and spatial variabilities of nutrients were determined through their dissolved inorganic forms.

While dissolved nutrients were mainly dominated by the Changjiang River source in the study area, they experienced various seasonal behaviors. Taking the DIN and DIP as examples, they behaved conservatively in the high-turbidity area, undergoing only physical dilution from the river channel to the river mouth (Figs. 8–9). Phytoplankton growth was quite weak in this area, and thus no significant nitrate was consumed. In the offshore region, DIN was consumed in the offshore side region of the sediment front during spring and summer (Fig. 8a–b), causing a sharp decrease over there. However, since the DIN was not the limiting factor in this system, the concentrations in the offshore region of the sediment front were still high, 40–70 mmol N/m^3 in summer (Fig. 8b) and 10–30 mmol N/m^3 in winter (Fig. 8d). With the eastward extension of the sediment front in autumn and winter, the DIN reached the offshore region as a result of advection (Fig. 8c–d).

DIP, on the other hand, was the limiting dissolved nutrient in the ecosystem of the Changjiang Estuary and adjacent regions (Gao and Song, 2005; Zhou et al., 2017). In addition to riverine sources, local mixing, pelagic and benthic bacterial mediated degradation were also the significant sources of DIP, causing DIP varying with the stratification status. DIP produced by these dynamics had the similar distribution patterns as the surface sediment. Phytoplankton growth consumed most of DIP in the water column during spring, summer and autumn, forming the same boundary of DIP and SSC at the sea surface in these three seasons (Fig. 9a–c). Outside the sediment front, the concentration of DIP was quite low, indicating DIP was depleted due to the growth of phytoplankton. In winter, the concentration of DIP increased in the offshore area due to vertical mixing and weak growth of phytoplankton (Fig. 9d), and similar behavior was seen in DIN in the offshore area (Fig. 8d). In winter, vertical mixing provided more dissolved nutrients to the upper column (Figs. 8d and 9d) and supported the growth of phytoplankton offshore in Zhejiang, where the suspended sediment concentration was relatively low.

Vertical mixing in the offshore region played an important role in the seasonal regulation of sediment, phytoplankton and dissolved nutrients as mentioned above. Thus, a vertical section from the river mouth to the offshore region was selected to investigate the seasonal variability of the vertical distribution (blue dashed line in Fig. 3). On this transect, the SSC in the upper layer of the offshore region increased from summer to winter (Fig. 10e, i and m) due to the decrease in stratification and higher resuspension driven by the increasing vertical mixing (Fig. 10h, l and p). The highest concentration of Chl-*a* in the low-turbidity upper column represented the spring bloom of phytoplankton (Fig. 10b). The DIP distribution showed a distinct low-value zone due to the consumption by phytoplankton in the upper column (Fig. 10c).

In summer, the stratification was strongest (Fig. 10h), resulting in the lowest sediment concentrations in the upper water column (Fig. 10e). Under this weak-mixing condition, the DIP in the upper column was depleted after the spring bloom and not replenished via vertical mixing (Fig. 10g), this dissolved nutrient limiting decreased the phytoplankton growth at the surface. Under these conditions, a subsurface Chl-*a* maximum developed (Fig. 10f).

With stronger vertical mixing from autumn to winter, and additional remineralization of detritus from dead phytoplankton, zooplankton and other biological components, the concentration of DIP reached its peak in winter. The whole water column became well mixed with DIP concentrations reaching ~0.8 mmol P/m^3.

In summary, the interactions between the physical and biogeochemical processes modulated the seasonal variabilities of dissolved nutrients and phytoplankton around the offshore area. The sediment dynamics confined the light penetration in the water column, which dominated the boundary of phytoplankton growth. Vertical mixing in the different seasons led to different dissolved nutrient supplies regimes, with river supplies becoming less important in autumn and winter.

Although dissolved nutrients were the major components of nutrient states, it should be noted that besides the dissolved form, the particulate nutrients, both organic and inorganic form, also contributed to the nutrient cycle, especially for the phosphorus (Liu et al., 2016). The particulate nutrients had much more complex dynamics, such as interaction with suspended sediment particles. Since most of available measurements for nutrients in this study were based on dissolved form, the only dynamics of dissolved nutrients were examined. The particulate nutrients should be resolved if one needs to understand full dynamics of nutrients on all forms.

5. Discussion

5.1. Interpretation from remote sensing data

Remote sensing from satellite platforms has been recognized as a useful method to retrieve surface SPM and Chl-*a* (O'Reilly et al., 1998; Shen et al., 2010). Using the semi-empirical radiative transfer (SERT) algorithm with physical based empirical coefficients (Shen et al., 2010), the snapshot for the Changjiang Estuary and its adjacent regions at 07:16 am May 16, 2016 in the spring season illustrated the offshore extent of the SSC in Fig. 11a. It appeared that turbid water covered the whole coastal region with the typical sediment concentration of ~500 mg/l. In the offshore region, the concentrations declined to 20–50 mg/l, where light penetrated into the water column and promote phytoplankton growth.

Chl-*a* was mostly observed in the offshore region (Fig. 11b), where relatively low-turbidity water presented (Fig. 11a). In the turbidity maximum and coastal high-turbidity regions, the concentration of Chl-*a* was low due to light limitation. The front between the high-, and low-turbidity water acted like a boundary for phytoplankton growth, which demonstrated the sediment's modulation of phytoplankton dynamics. The location of modeled high Chl-*a* in spring matched the spot where historical spring bloom was observed (Gao and Song, 2005; Zhu et al., 2009; Guo et al., 2014). The distribution of Chl-*a* concentration showed a narrow band off the sediment front in May.

The snapshots of SPM and Chl-*a* from remote sensing also revealed the existence of small-scale structures along the sediment front. These fine structures suggested the existence of eddies along the low-salinity front. Chen et al. (2008) proposed that such eddies were produced by baroclinic instabilities due to the salinity-induced density gradient. These eddies also led to some isolated patches of high-turbidity water, causing detachment occurred, then resulting in the horizontal mixing of coastal high-turbidity water and offshore low-turbidity water. it was

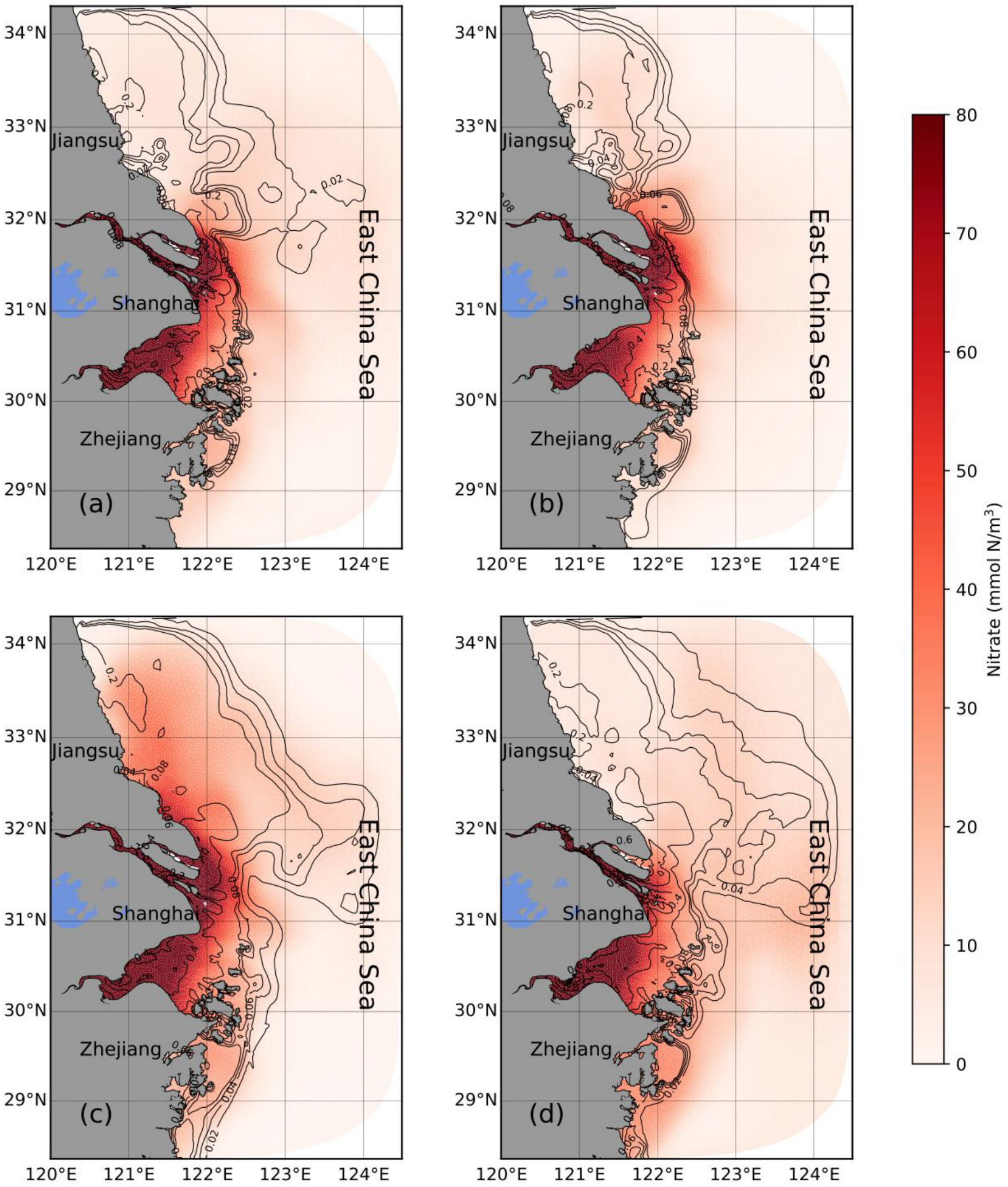

Fig. 8. Seasonal-averaged surface distributions of suspended sediment concentration (contour, unit: g/l) and DIN (colored image, unit: mmol N/m^3) during spring (a), summer (b), autumn (c) and winter (d). (For interpretation of the references to color in this figure legend, the reader is referred to the web version of this article.)

partially responsible for the supply of dissolved nutrients that supported that narrow diatom patch along the front. The snapshot from remote sensing showed that sediment-phytoplankton interactions exhibited much more complicated temporal and spatial variations on tidal or wind-event scales. This was a mechanism presented in the model and it was responsible for the supply of dissolved nutrients that supported that narrow diatom patch along the front over a short time scale. This eddy-induced water exchange between inner and outer regions of the front was revealed also in previous studies (Chen et al., 2008; Ge et al., 2015a). However, it should be noted that these structures have been smoothened during the temporally-averaging on the seasonal scale shown in Figs. 6–9.

5.2. Influence of ocean circulation

Besides the regulation effect that riverine sediment or locally resuspended sediment had on phytoplankton and nutrient dynamics, the oceanic flow also played an important role in the offshore dynamics of the pelagic ecosystem. The Taiwan Warm Current (TWC) is the strongest oceanic intrusion in the offshore region of the Changjiang Estuary, influencing the physical and biogeochemical conditions.

In summer, the TWC reached the Changjiang Estuary, with seasonal-

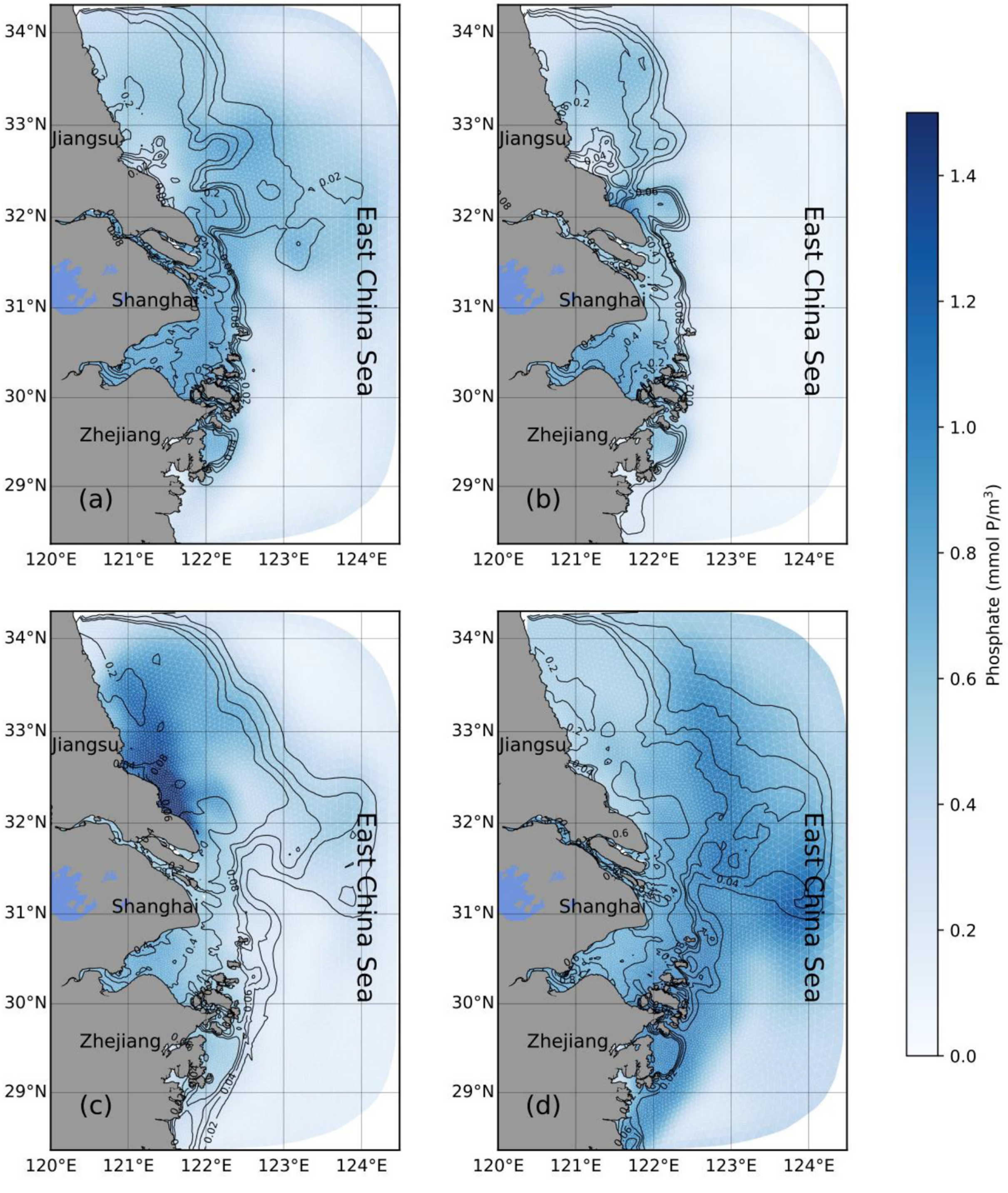

Fig. 9. Seasonal-averaged surface distributions of suspended sediment concentration (contour, unit: g/l) and DIP (colored image, unit: mmol P/m^3) during spring (a), summer (b), autumn (c) and winter (d). (For interpretation of the references to color in this figure legend, the reader is referred to the web version of this article.)

averaged velocities of ~0.1 m/s in the bottom layer (~40–50 m) (Fig. 12a). This current carried high-temperature water from the south to the north. Additionally, the intrusion of TWC and Kuroshio were recognized as a water mass with relatively higher DIP concentration in the bottom column, compared with adjacent shelf water (Chen et al., 2003b; Zhou et al., 2017). These higher-DIP water from intrusion and its induced upwelling partly supported the dinoflagellate bloom in the coastal region (Zhou et al., 2019). Along the selected dashed line in Fig. 12a, the SSC was relatively low, < 10 mg/l in the offshore area (Fig. 12b), indicating the SPM had s weak effect on the biogeochemical process in this area. While there was low DIP concentration of < 0.1 mmol/m^3 in the surface water, the TWC contributed to higher DIP in bottom (> 0.6 mmol/m^3), thus vertically stratified DIP distribution was seen from Fig. 12c with additive effect from summer stratification in water column discussed in Section 4. Due to low SPM, the light reached subsurface layer (~25–30 m), and enabled the development of a subsurface Chl-*a* maximum where the nutrients were adequate for phytoplankton growth (Fig. 12c), which matches well with previous measurements in Chen et al. (2003b). Previous observations also indicated that the DIP from the TWC played a critical role in the maintenance of dinoflagellate blooms here (Zhou et al., 2017).

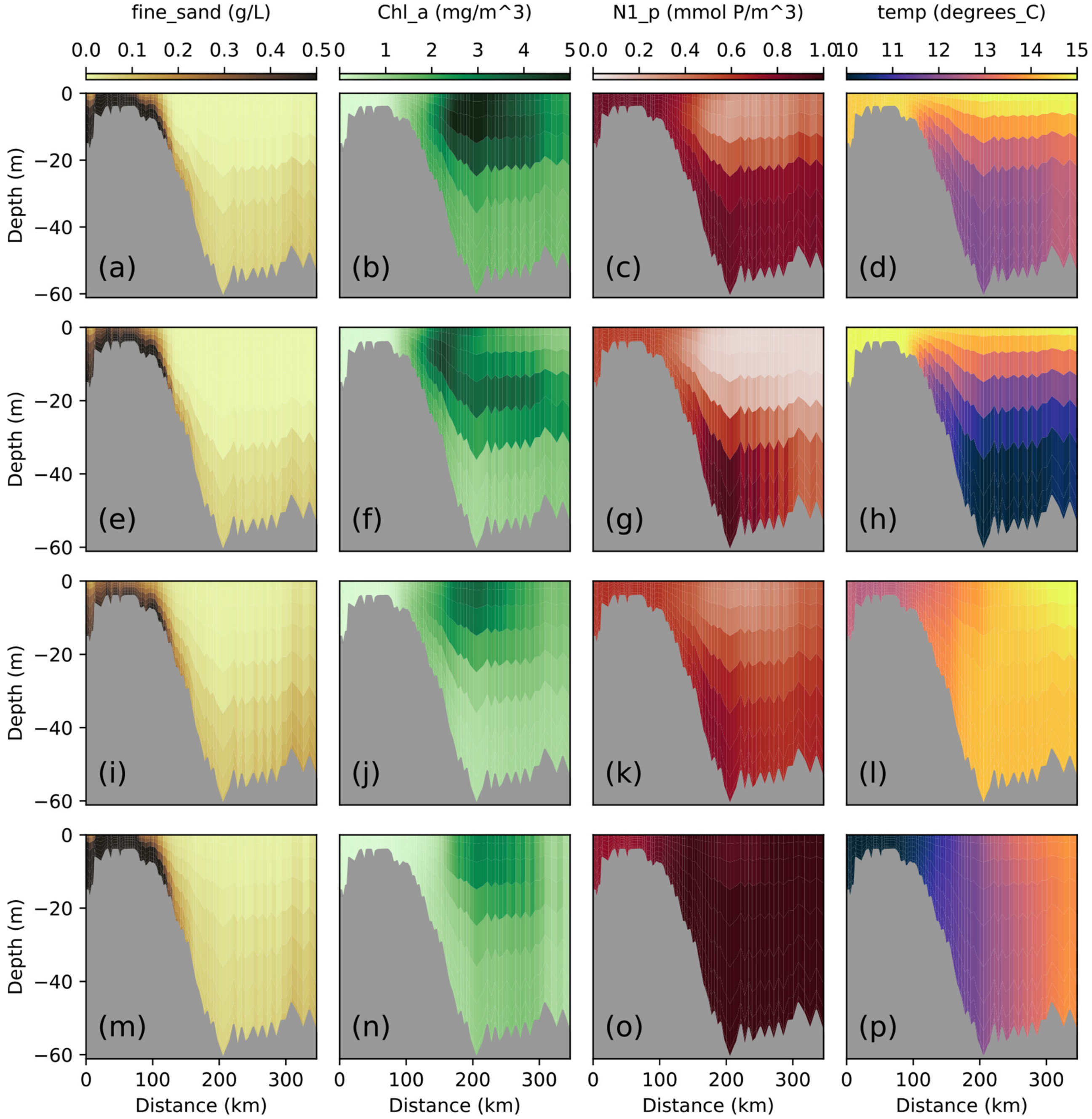

Fig. 10. Seasonal-averaged vertical distributions of the suspended sediment concentration (first column, unit: g/l), phytoplankton (second column, unit: mg/m^3), DIP (third column, unit: mmol P/m^3), and temperature (forth column, unit: degree) on the selected section during spring (a–d), summer (e–h), autumn (i–l) and winter (m–p).

5.3. Zooplankton impact

Phytoplankton biomass are not the only functional groups depending on nutrients and light. There are four phytoplankton, three zooplankton and one bacteria functional groups in ERSEM model, so the competition (for resources, i.e. nutrients) and predation also plays a role. Low summer diatoms biomass generally reflects both higher predation pressure from zooplankton and competition from smaller phytoplankton and bacteria which have higher growth rates and smaller sedimentation rates. In fact, zooplankton predation together with nutrient depletion contributes to the demise of the diatom spring bloom.

The model results showed that the total zooplankton biomass (mesozooplankton, microzooplankton and heterotrophic flagellates) on the seasonal scale mainly followed the distribution of phytoplankton, namely higher concentrations during spring and summer, and lower concentrations in autumn and winter (Fig. 13). Zooplankton dominated the larger offshore areas of the sediment front, reaching the outer shelf where non-diatom biomass was adequate to be predated. Meanwhile, low zooplankton concentration (< 70 mg C/m^3) was found within the coastal region in all seasons.

5.4. Stability of seasonal structures

The model simulation covered the time period from 1999 to 2016. Besides the atmospheric and oceanic variabilities that caused the model fluctuations, the major influencing factor for the Changjiang Estuary and adjacent region could be the construction of the Three Gorges Dam. It became operational in 2003, and caused very strong sedimentation

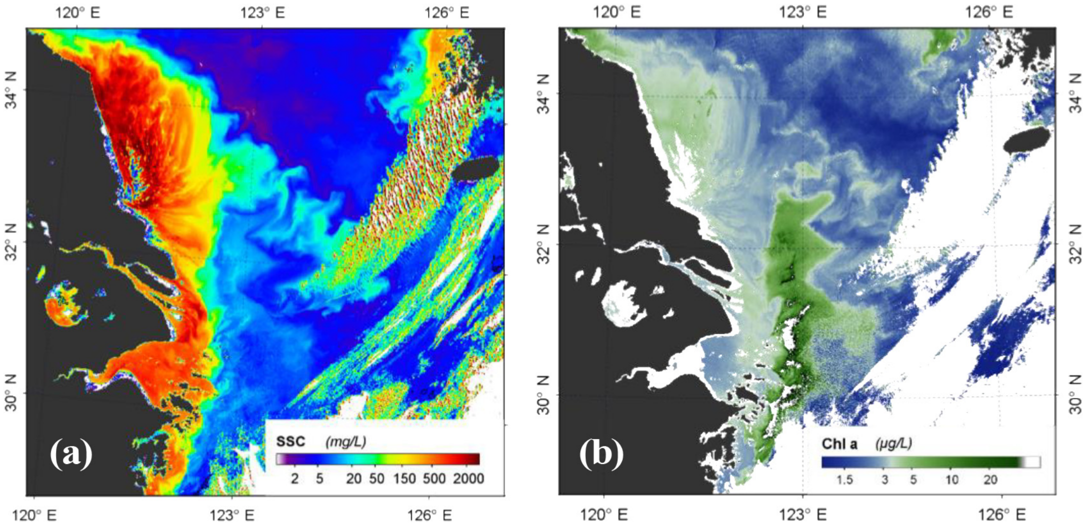

Fig. 11. Distributions of the GOCI-retrieved surface sediment concentration (a) and Chl-*a* (b) around the Changjiang Estuary from the snapshot at 15:30 PM, May 16th, 2016.

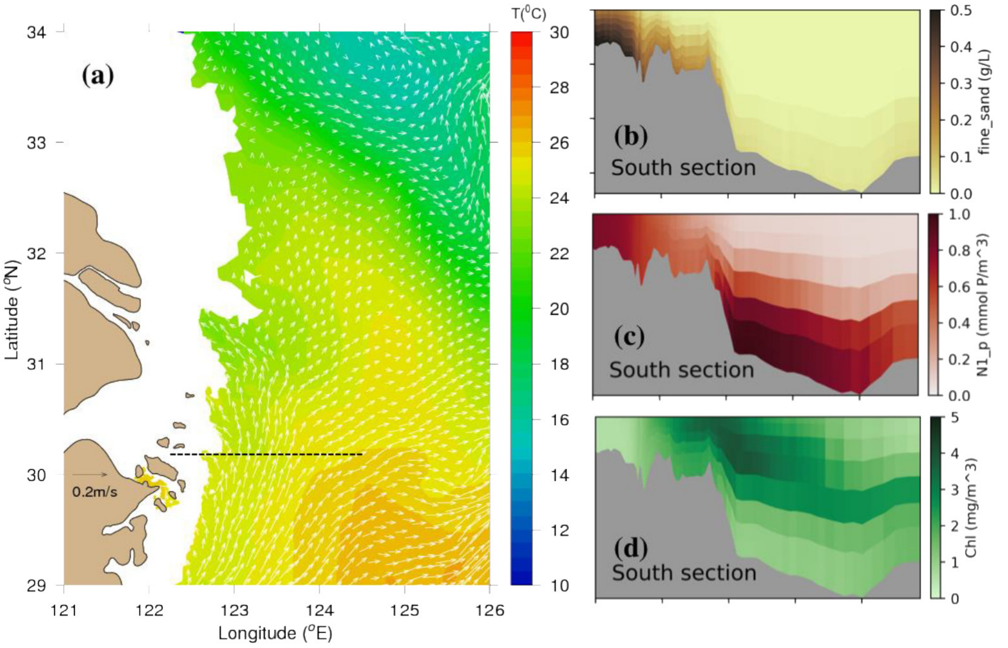

Fig. 12. Seasonal-averaged flow vectors and temperature at 40-m depth (a) in summer. Vertical distribution of SPM (b), phosphate (c) and Chl-*a* (d) along the dashed-line section shown in (a).

impact on the lower reach of the Changjiang river. The sediment concentration into the estuary has significant decreased, as well as the annual sediment load (Luan et al., 2016; Yang et al., 2015). However, the decrease in sediment concentration mainly occurred in the river channel from Datong station to river mouth. The offshore region, particularly around the sediment front region in this study, did not show significant variation trend based on continuous remote sensing from 2003 to 2010 (Shen et al., 2013). It mainly indicated a local temporal oscillation. The annual freshwater flux before and after the construction of the Three Gorges Dam were of the same amplitude (Luan et al., 2016).

Since the freshwater discharge and offshore sediment concentration did not change significantly, the seasonality of dissolved nutrients and phytoplankton has remained relatively stable before and after the operation of Three Gorges Dam. The magnitude of nutrient and phytoplankton concentration surely has some oscillation, which probably was still caused by increasing use of fertilizers.

5.5. Stoichiometry in sediment and nutrients

Nutrients entering the estuarine environment, with an additional contribution from submarine groundwater discharges, can undergo rapid adsorption into suspended sediments with the potential to conversely have desorption processes during transportation and resuspension, or even deposit into sea bed (Wang et al., 2018; Liu et al., 2017, 2018). It should be noted that the absorption and desorption of nutrients in the suspended particulate matters were not included in the ERSEM. Nutrients were treated as dissolved and particulate states in the biogeochemical model. Based on previous experiments, the nitrate has weak capacity on absorption and desorption in sediment, whereas the phosphate has notable absorption and desorption processes with suspended sediment. In future studies, the sediment's biogeochemical

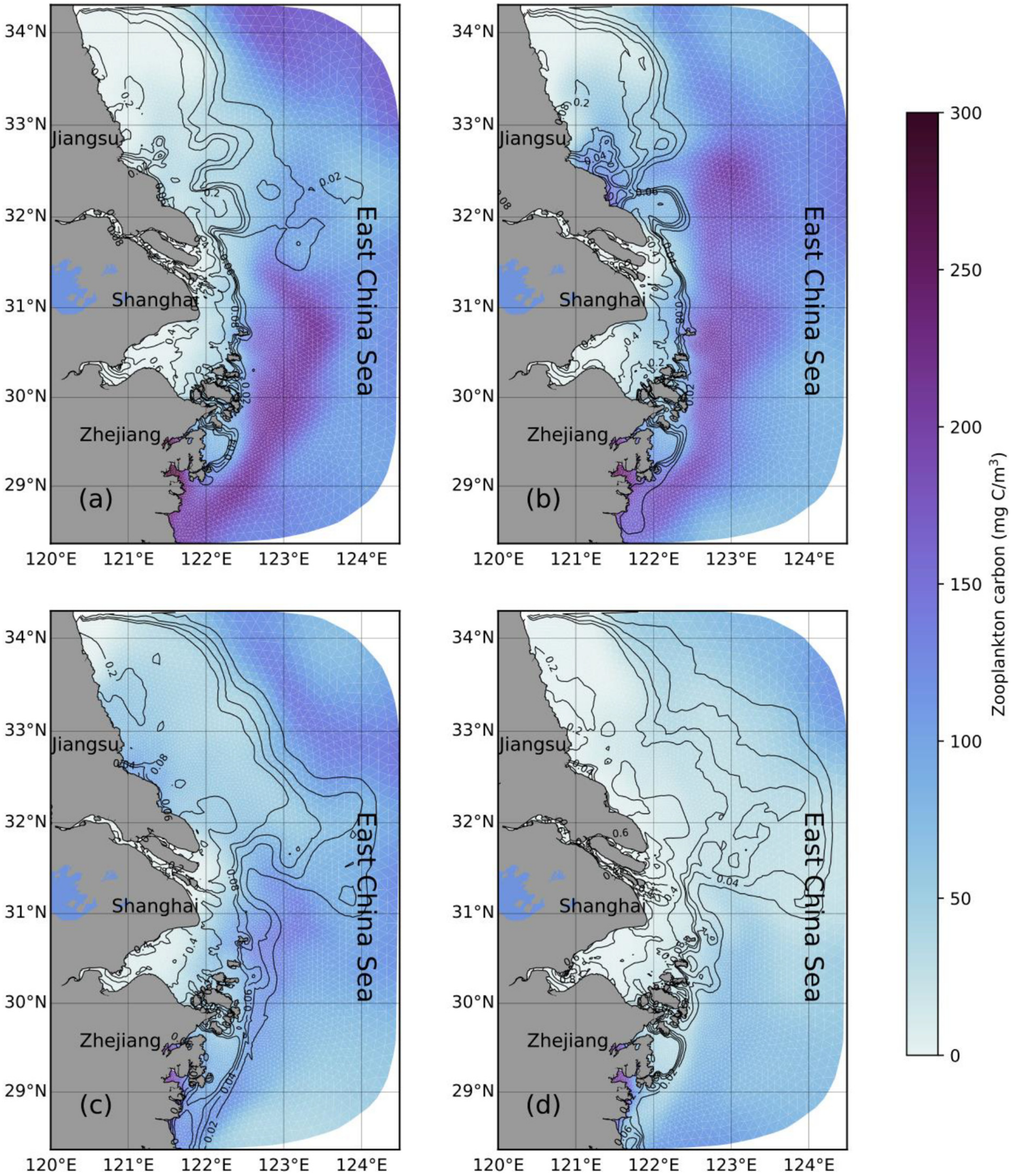

Fig. 13. Seasonal-averaged surface distributions of the suspended sediment concentration (contour) and total biomass of zooplankton (colored image) during spring (a), summer (b), autumn (c) and winter (d). (For interpretation of the references to color in this figure legend, the reader is referred to the web version of this article.)

process should be included in whole nutrient cycle, particularly the adsorption/desorption behavior for phosphorus, given its great importance in high-turbidity environments such as the Changjiang Estuary and adjacent coastal regions.

6. Summary

In this study, a coupled physical-biogeochemical model system, based on FVCOM and ERSEM, was developed to examine the impact of the sediment front on the nutrients and phytoplankton dynamics over the inner shelf of the ECS off the high-turbidity Changjiang Estuary. The model system successfully revealed the variation of Chl-*a* in the offshore region, reproducing the major variability modes of various physical and biogeochemical variables obtained from the seasonal field campaigns as seen in PCA. The model results revealed that the suspended sediments played a role in regulating the growth of phytoplankton. Influenced by the seasonal variations in the extension of low-salinity water, which carried nutrients and sediment, the phytoplankton followed the sediment front from more onshore locations during spring and summer to further offshore locations during autumn and winter. Results demonstrated that diatoms were major contributors to Chl-*a* concentration, but lower biomass contribution to total phytoplankton carbon, and non-diatoms (i.e. dinoflagellates etc.) dominated out of the sediment front, and extended to the outer shelf region.

DIN and DIP had different behaviors on the seasonal scale. Nitrate behavior could generally be approximated by physical dilution and transport of freshwater discharge, and remained high offshore of the sediment front. Whereas phosphate, acting as the limiting nutrient in the ecosystem, showed more local dynamics and reached lower concentrations offshore of the front. It's implied from the vertical profiles that vertical mixing largely controlled sediment re-suspension, nutrient mixing and phytoplankton distribution in the offshore water column.

Acknowledgement

J. Ge, P. Ding, F. Shen and Y. Xu were supported by the National Key Research and Development Program of China (Grant No. 2016YFA0600903) and the National Natural Science Foundation of China (Grant No. 41776104, 41606025). J. Liu and R. Bellerby was supported by SKLEC-2016RCDW01. R. Torres and J. Bruggeman were supported by the H2020 TAPAS project, as well as by National Environment Research Council grant CACOON. Dr. Xiaodao Wei helped process the GOCI satellite data; Ms. Shenyang Shi helped perform the PCA analysis. All datasets supporting this study are publicly available at https://figshare.com/s/243b4e8417b7bd0106d8.

References

Allen, J.I., Somerfield, P.J., 2009. A multivariate approach to model skill assessment. J. Mar. Syst. 76 (1), 83–94. https://doi.org/10.1016/j.jmarsys.2008.05.009.

Barbosa, A.B., Domingues, R.B., Galvão, H.M., 2009. Environmental Forcing of Phytoplankton in a Mediterranean Estuary (Guadiana Estuary, South-western Iberia): A Decadal Study of Anthropogenic and Climatic Influences. Estuar. Coasts 33 (2), 324–341. https://doi.org/10.1007/s12237-009-9200-x.

Beardsley, R.C., Chen, C., Xu, Q., 2013. Coastal flooding in Scituate (MA): a FVCOM study of the 27 December 2010 nor'easter. J. Geophys. Res. Oceans 118 (11), 6030–6045. https://doi.org/10.1002/jgrc.20443.

Boynton, W.R., Ceballos, M.A.C., Bailey, E.M., Hodgkins, C.L.S., Humphrey, J.L., Testa, J.M., 2018. Oxygen and nutrient exchanges at the sediment-water interface: a global synthesis and critique of estuarine and coastal data. Estuar. Coasts 41 (2), 1–33. https://doi.org/10.1007/s12237-017-0275-5.

Bruggeman, J., Bolding, K., 2014. A general framework for aquatic biogeochemical models. Environ. Model. Softw. 61 (C), 249–265. https://doi.org/10.1016/j.envsoft.2014.04.002.

Butenschon, M., Clark, J., Aldridge, J.N., Allen, J.I., Artioli, Y., Blackford, J., et al., 2016. ERSEM 15.06: a generic model for marine biogeochemistry and the ecosystem dynamics of the lower trophic levels. Geosci. Model Dev. 9 (4), 1293–1339. https://doi.org/10.5194/gmd-9-1293-2016-supplement.

Cazenave, P.W., Bedington, M., 2018. PyFVCOM (Version 2.1.3) [Software]. Plymouth Marine Laboratory, Plymouth, Devon, United Kingdom. https://doi.org/10.5281/zenodo.1422462.

Chen, C., Beardsley, R.C., Limeburner, R., 1994. Comparison of winter and summer hydrographic observations in the Yellow and East China Seas and adjacent Kuroshio during 1986. Cont. Shelf Res. 14, 909–929.

Chen, C., Liu, H., Beardsley, R.C., 2003a. An unstructured, finite-volume, three-dimensional, primitive equation ocean model: application to coastal ocean and estuaries. J. Atmos. Ocean. Technol. 20, 159–186.

Chen, C., Zhu, J., Beardsley, R.C., Franks, P.S., 2003b. Physical-biological sources for the Dense Algal Bloom over the Western Shelf of the East China Sea. Geophysical Research Letter 30 (10), 1515 22–1:4.

Chen, C., Wang, L., Ji, R., Budd, J.W., Schwab, D.J., Beletsky, D., Fahnenstiel, G.L., Vanderploeg, H.A., Eadie, B.J., Cotner, J., 2004. Impacts of suspended sediment on the ecosystem in Lake Michigan: a comparison between the 1998 and 1999 plume events. Journal of Geophysical Research 109 (C10S05), 18.

Chen, C., Beardsley, R.C., Cowles, G., 2006. An unstructured grid, finite-volume coastal ocean model (FVCOM) system. Special issue entitled "advance in computational oceanography". Oceanography 19 (1), 78–89.

Chen, C., Xue, P., Ding, P., Beardsley, R.C., Xu, Q., Mao, X., Gao, G., Qi, J., Li, C., Lin, H., Cowles, G., Shi, M., 2008. Physical mechanisms for the offshore detachment of the Chanjiang diluted water in the East China Sea. J. Geophys. Res. 113, C02002. https://doi.org/10.1029/2006JC003994.

Chen, C., Beardsley, R.C., Cowles, G., Qi, J., Lai, Z., Gao, G., Stuebe, D., Xu, Q., Xue, P., Ge, J., Ji, R., Hu, S., Tian, R., Huang, H., Wu, L., Lin, H., Sun, Y., Zhao, L., 2013. An Unstructured Grid, Finite-Volume Community Ocean Model FVCOM User Manual, SMAST/UMASSD Technical Report 13-0701, School of Marine Science and Technology. University of Massachusetts-Dartmouth, New Bedford, MA, USA.

Choi, J.K., Park, Y.J., Ahn, J.H., Lim, H.S., Eom, J., Ryu, J.H., 2012. GOCI, the world's first geostationary ocean color observation satellite, for the monitoring of temporal variability in coastal water turbidity. J. Geophys. Res. 117, C09004. https://doi.org/10.1029/2012JC008046.

Choi, J.K., Min, J.E., Noh, J.H., Han, T.H., Yoon, S., Park, Y.J., Moon, J.E., Ahn, J.H., Ahn, S.M., Park, J.H., 2014. Harmful algal bloom (HAB) in the East Sea identified by the Geostationary Ocean Color Imager (GOCI). Harmful Algae 39, 295–302.

CWRC (Changjiang Water Resources Commission), 2011. Changjiang sediment bulletin. available at: http://www.cjh.com.cn/pages/nsgb.html (in Chinese).

de Swart, H.E., Schuttelaars, H.M., Talke, S.A., 2009. Initial growth of phytoplankton in turbid estuaries: a simple model. Cont. Shelf Res. 29 (1), 136–147. https://doi.org/10.1016/j.csr.2007.09.006.

Donohue, I., Garcia Molinos, J., 2009. Impacts of increased sediment loads on the ecology of lakes. Biol. Rev. 84 (4), 517–531. https://doi.org/10.1111/j.1469-185X.2009.00081.x.

Ebenhoh, W., Kohlmeier, C., Radford, P.J., 1995. The benthic bio-logical model in the European regional seas ecosystem model. Neth. J. Sea Res. 33, 423–452.

Egbert, G.D., Erofeeva, S.Y., 2002. Efficient inverse modeling of barotropic ocean tides. J. Atmos. Ocean. Technol. 19 (2), 183–204.

Franklin, H.M., Garzon-Garcia, A., Burton, J., Moody, P.W., De Hayr, R.W., Burford, M.A., 2018. A novel bioassay to assess phytoplankton responses to soil-derived particulate nutrients. Sci. Total Environ. 636, 1470–1479. https://doi.org/10.1016/j.scitotenv.2018.04.195.

Friedl, G., Wüest, A., 2002. Disrupting biogeochemical cycles - consequences of damming. Aquat. Sci. 64, 55. https://doi.org/10.1007/s00027-002-8054-0.

Furuya, K., Kurita, K., Odate, T., 1996. Distribution of phytoplankton in the East China Sea in the winter of 1993. J. Oceanogr. 52, 323–333. https://doi.org/10.1007/BF02235927.

Furuya, K., Hayashi, M., Yabushita, Y., Ishikawa, A., 2003. Phytoplankton dynamics in the East China Sea in spring and summer as revealed by HPLC-derived pigment signatures. Deep-Sea Res. Pt. II 50, 367–387. https://doi.org/10.1016/S0967-0645(02)00460-5.

Gao, X., Song, J., 2005. Phytoplankton distributions and their relationship with the environment in the Changjiang Estuary, China. Marine Pollution Bulletin 50 (3), 327–335. https://doi.org/10.1016/j.marpolbul.2004.11.004.

Gao, L., Li, D., Zhang, Y., 2012. Nutrients and particulate organic matter discharged by the Changjiang (Yangtze River): Seasonal variations and temporal trends. J. Geophys. Res. Biogeosci. 117 (G), G04001. https://doi.org/10.1029/2012JG001952.

Ge, J., Ding, P., Chen, C., Hu, S., Fu, G., Wu, L., 2013. An integrated East China Sea–Changjiang estuary model system with aim at resolving multi-scale regional–-shelf–estuarine dynamics. Ocean Dyn. 63 (8), 881–900. https://doi.org/10.1007/s10236-013-0631-3.

Ge, J., Chen, C., Ding, P., 2015a. Estimation of critical shear stress for erosion in the Changjiang Estuary: a synergy research of observation, GOCI sensing and modeling. J. Geophys. Res. Oceans 120 (1), 8439–8465. https://doi.org/10.1002/2015JC010992.

Ge, J., Ding, P., Chen, C., 2015b. Low-salinity plume detachment under non-uniform summer wind off the Changjiang Estuary. Estuarine, Coastal and Shelf Science 156 (C), 61–70. https://doi.org/10.1016/j.ecss.2014.10.012.

Ge, J., Zhou, Z., Yang, W., Ding, P., Chen, C., Wang, Z.B., Gu, J., 2018. Formation of concentrated benthic suspension in a time-dependent salt wedge estuary. J. Geophys. Res. Oceans 123 (11), 8581–8607. https://doi.org/10.1029/2018JC013876.

Geider, R.J., MacIntyre, H.L., Kana, T.M., 1997. A dynamic model of phytoplankton growth and acclimation: responses of the balanced growth rate and the chlorophyll a:carbon ratio to light, nutrient-limitation and temperature. Mar. Ecol. Prog. Ser. 148, 187–200.

Guo, S., Feng, Y., Wang, L., Dai, M., Liu, Z., Bai, Y., Sun, J., 2014. Seasonal variation in the phytoplankton community of a continental-shelf sea: the East China Sea. Mar. Ecol. Prog. Ser. 516, 103–126. https://doi.org/10.3354/meps10952.

He, X., Bai, Y., Pan, D., Huang, N., Dong, X., Chen, J., et al., 2013. Using geostationary satellite ocean color data to map the diurnal dynamics of suspended particulate matter in coastal waters. Remote Sens. Environ. 133 (C), 225–239. https://doi.org/10.1016/j.rse.2013.01.023.

He, Q., Qiu, Y., Liu, H., Sun, X., Kang, L., Cao, L., et al., 2017. New insights into the impacts of suspended particulate matter on phytoplankton density in a tributary of the Three Gorges Reservoir, China. Scientific Reports 7 (1), 1–11. https://doi.org/10.1038/s41598-017-13235-0.

Hu, C., Feng, L., Lee, Z.P., 2012. Evaluation of GOCI sensitivity for at-sensor radiance and GDPS-retrieved chlorophyll-a products. Ocean Science Journal 47 (3), 279–285.

Hu, B., Wang, P., Zhang, N., Wang, C., Ao, Y., 2016. Photoproduction of dissolved organic carbon and inorganic nutrients from resuspended lake sediments. Environ. Sci. Pollut. Res. 23 (21), 1–10. https://doi.org/10.1007/s11356-016-7327-4.

Huettel, M., Berg, P., Kostka, J.E., 2014. Benthic exchange and biogeochemical cycling in permeable sediments. Annu. Rev. Mar. Sci. 6 (1), 23–51. https://doi.org/10.1146/annurev-marine-051413-012706.

Ji, R., Chen, C., Budd, J., Schwab, D., Beletsky, D., Fahanenstial, D., Johengen, T.H., Lavrentyev, H., Eadies, B., Cotner, J., Gardner, W., Bundy, M., 2002. A coupled biological and physical model study of the ecosystem in Lake Michigan part II: influence of suspended sediment. Ecol. Model. 152, 169–190.

Jiang, T., Yu, Z.M., Song, X.X., Cao, X.H., Yuan, Y.Q., 2010. Long-term ecological interactions between nutrient and phytoplankton community in the Changjiang estuary. Chin. J. Oceanol. Limnol. 28, 887–898.

Jiang, Z., Chen, J., Zhou, F., Shou, L., Chen, Q., Tao, B., et al., 2015. Controlling factors of summer phytoplankton community in the Changjiang (Yangtze River) Estuary and adjacent East China Sea shelf. Cont. Shelf Res. 101, 1–14. https://doi.org/10.1016/j.csr.2015.04.009.

Kang, Y., Song, X., Liu, Z., 2012. Sediment resuspension dampens the effect of nutrient inputs on the phytoplankton community: a mesocosm experiment study. Hydrobiologia 710 (1), 117–127. https://doi.org/10.1007/s10750-012-1221-y.

Klausmeier, C.A., Litchman, E., Daufresne, T., Levin, S., 2008. Phytoplankton stoichiometry. Ecol. Res. 23, 479–485.

Lamquin, N., Mazeran, C., Doxaran, D., Ryu, J.H., Park, Y.J., 2012. Assessment of GOCI radiometric products using MERIS, MODIS and field measurements. Ocean Science Journal 47 (3), 287–311.

Li, M., Xu, K., Watanabe, M., Chen, Z., 2007. Long-term variations in dissolved silicate, nitrogen, and phosphorus flux from the Yangtze River into the East China Sea and impacts on estuarine ecosystem. Estuar. Coast. Shelf Sci. 71 (1–2), 3–12. https://doi.org/10.1016/j.ecss.2006.08.013.

Liu, S.-M., Qi, X.H., Li, X., Ye, H.R., Wu, Y., Ren, J.L., et al., 2016. Nutrient dynamics from the Changjiang (Yangtze River) estuary to the East China Sea. J. Mar. Syst. 154 (Part A), 15–27. https://doi.org/10.1016/j.jmarsys.2015.05.010.

Liu, J., Su, N., Wang, X., Du, J., 2017. Submarine groundwater discharge and associated nutrient fluxes into the southern Yellow Sea: a case study for semi-enclosed and oligotrophic seas-implication for green tide bloom. J. Geophys. Res. Oceans 122 (1), 139–152. https://doi.org/10.1002/2016JC012282.

Liu, J., Du, J., Wu, Y., Liu, S., 2018. Nutrient input through submarine groundwater discharge in two major Chinese estuaries: the Pearl River Estuary and the Changjiang River Estuary. Estuar. Coast. Shelf Sci. 203, 17–28. https://doi.org/10.1016/j.ecss.2018.02.005.

Luan, H.L., Ding, P.-X., Wang, Z.B., Ge, J.-Z., Yang, S.-L., 2016. Decadal morphological evolution of the Yangtze Estuary in response to river input changes and estuarine engineering projects. Geomorphology 265 (C), 12–23. https://doi.org/10.1016/j.geomorph.2016.04.022.

Luo, Z., Zhu, J., Wu, H., Li, X., 2017. Dynamics of the sediment plume over the Yangtze Bank in the Yellow and East China Seas. Journal of Geophysical Research: Oceans 122, 10,073–10,090. https://doi.org/10.1002/2017JC013215.

May, C.L., Koseff, J., Lucas, L.V., Cloern, J.E., Schoellhamer, D.H., 2003. Effects of spatial and temporal variability of turbidity on phytoplankton blooms. Mar. Ecol. Prog. Ser. 254, 111–128. https://doi.org/10.3354/meps254111.

Moore, W.S., 2006. The role of submarine groundwater discharge in coastal biogeochemistry. J. Geochem. Explor. 88, 389–393.

Moore, W.S., 2010. The effect of submarine groundwater discharge on the ocean. Annu. Rev. Mar. Sci. 2 (1), 59–88. https://doi.org/10.1146/annurev-marine-120308-081019.

Niemistö, J., Kononets, M., Ekeroth, N., Tallberg, P., Tengberg, A., Hall, P.O.J., 2018. Benthic fluxes of oxygen and inorganic nutrients in the archipelago of Gulf of Finland, Baltic Sea – effects of sediment resuspension measured in situ. J. Sea Res. 135, 95–106. https://doi.org/10.1016/j.seares.2018.02.006.

Olsen, A., Key, R.M., van Heuven, S., Lauvset, S.K., Velo, A., Lin, X., Schirnick, C., Kozyr, A., Tanhua, T., Hoppema, M., Jutterstrom, S., Steinfeldt, R., Jeansson, E., Ishii, M., Perez, F.F., Suzuki, T., 2016. The Global Ocean Data Analysis Project version 2 (GLODAPv2)—aninternally consistent data product for the world ocean. Earth Syst Sci Data 8, 297–323. https://doi.org/10.5194/essd-8-297-2016.

O'Reilly, J.E., Maritorena, S., Mitchell, B.G., Siegel, D.A., Carder, K.L., Garver, S.A., Kahru, M., McClain, C., 1998. Ocean color chlorophyll algorithm for SeaWiFS. J. Geophys. Res. 103 (C11), 24937–24953.

Piwowarczyk, L., Bishop, H., Saia, K., Crosby, S., Mudymba, F.T., Hashi, N.I., Raj, A., 2016. Application of GOCI satellite data to ocean modeling. J. Coastal Res. 15 (1), 1409–1414.

Qi, J., Chen, C., Beardsley, R., Perrie, W., Cowles, G., Lai, Z., 2009. An unstructured-grid finite-volume surface wave model (FVCOM-SWAVE): implementation, validations and applications. Ocean Model. 28 (1–3), 153–166.

Qi, J., Chen, C., Beardsley, R.C., 2018. FVCOM one-way and two-way nesting using ESMF_ development and validation. Ocean Model. 124, 94–110. https://doi.org/10.1016/j.ocemod.2018.02.007.

Ryu, J.-H., Han, H.-J., Cho, S., Park, Y.-J., Ahn, Y.-H., 2012. Overview of geostationary ocean color imager (GOCI) and GOCI data processing system (GDPS). Ocean Science Journal 47 (3), 223–233. https://doi.org/10.1007/s12601-012-0024-4.

Sadat-Noori, M., Santos, I.R., Tait, D.R., Maher, D.T., 2016. Fresh meteoric versus recirculated saline groundwater nutrient inputs into a subtropical estuary. Science of the Total Environment, the 566–567 (C), 1440–1453. https://doi.org/10.1016/j.scitotenv.2016.06.008.

Shen, F., Verhoef, W., Zhou, Y., Salama, M.S., Liu, X., 2010. Satellite estimates of wide-range suspended sediment concentrations in Changjiang (Yangtze) Estuary using MERIS data. Estuar. Coast. 33 (6), 1420–1429. https://doi.org/10.1007/s12237-010-9313-2.

Shen, F., Zhou, Y., Li, J., He, Q., Verhoef, W., 2013. Remotely sensed variability of the suspended sediment concentration and its response to decreased river discharge in the Yangtze estuary and adjacent coast. Cont. Shelf Res. 69 (C), 52–61. https://doi.org/10.1016/j.csr.2013.09.002.

Shi, Z., Xu, J., Huang, X., Zhang, X., Jiang, Z., Ye, F., Liang, X., 2017. Relationship between nutrients and plankton biomass in the turbidity maximum zone of the Pearl River Estuary. J. Environ. Sci. 57 (C), 72–84. https://doi.org/10.1016/j.jes.2016.11.013.

Siswanto, E., Tang, J., Yamaguchi, H., Ahn, Y.-H., Ishizaka, J., Yoo, S., et al., 2011. Empirical ocean-color algorithms to retrieve chlorophyll-a, total suspended matter, and colored dissolved organic matter absorption coefficient in the Yellow and East China Seas. J. Oceanogr. 67 (5), 627–650. https://doi.org/10.1007/s10872-011-0062-z.

Smagorinsky, J., 1963. General Circulation Experiments with the Primitive Equations. Mon. Weather Rev. 91, 99–164.

Sobolev, D., Moore, K., Morris, A.L., 2009. Nutrients and Light Limitation of Phytoplankton Biomass in a Turbid Southeastern Reservoir: Implications for Water Quality. Southeast. Nat. 8 (2), 255–266. https://doi.org/10.1656/058.008.0205.

Sokoletsky, L., Yang, X., Shen, F., 2014. In: Frouin, R.J., Pan, D., Murakami, H. (Eds.), MODIS-based Retrieval of Suspended Sediment Concentration and Diffuse Attenuation Coefficient in Chinese Estuarine and Coastal Waters. Vol. 9261. Presented at the SPIE Asia Pacific Remote Sensing, SPIE, pp. 926119. https://doi.org/10.1117/12.2069205.

Stow, C.A., Jolliff, J., McGillicuddy Jr., D.J., Doney, S.C., Allen, J.I., Friedrichs, M.A.M., et al., 2009. Skill assessment for coupled biological/physical models of marine systems. J. Mar. Syst. 76 (1–2), 4–15. https://doi.org/10.1016/j.jmarsys.2008.03.011.

Sun, X., Shen, F., Liu, D., Bellerby, R.G., Liu, Y., Tang, R., 2018. In situ and satellite observations of phytoplankton size classes in the entire continental Shelf Sea, China. J. Geophys. Res. Oceans 123 (5), 3523–3544.

Vanderploeg, H.A., Johengen, T.H., Lavrentyev, P.J., Chen, C., Lang, G.A., Agy, M.A., et al., 2007. Anatomy of the recurrent coastal sediment plume in Lake Michigan and its impacts on light climate, nutrients, and plankton. Journal of Geophysical Research 112 (C3), C03S90. https://doi.org/10.1029/2004JC002379.

Wang, X., Baskaran, M., Su, K., Du, J., 2018. The important role of submarine groundwater discharge (SGD) to derive nutrient fluxes into river dominated Ocean Margins – The East China Sea. Mar. Chem. 204, 121–132. https://doi.org/10.1016/j.marchem.2018.05.010.

Wang, Y., Wu, H., Gao, L., Shen, F., Liang, X.S., 2019. Spatial distribution and physical controls of the spring algal blooming off the Changjiang River estuary. Estuar. Coasts 42 (4), 1–18. https://doi.org/10.1007/s12237-019-00545-x.

Wu, L., Chen, C., Guo, P., Shi, M., Qi, J., Ge, J., 2011a. A FVCOM-based unstructured grid wave, current, sediment transport model, I Model description and validation. J. Ocean Univ. China 10 (1), 1–8. https://doi.org/10.1007/s11802-011-1788-3.

Wu, H., Zhu, J., Shen, J., Wang, H., 2011b. Tidal modulation on the Changjiang River plume in summer. J. Geophys. Res. 116 (C8), C08017. https://doi.org/10.1029/2011JC007209.

Yang, S.L., Xu, K.H., Milliman, J.D., Yang, H.F., Wu, C.S., 2015. Decline of Yangtze River water and sediment discharge: impact from natural and anthropogenic changes. Sci. Rep. 1–14. https://doi.org/10.1038/srep12581.

Zhou, M.-J., Shen, Z.-L., Yu, R.-C., 2008. Responses of a coastal phytoplankton community to increased nutrient input from the Changjiang (Yangtze) river. Cont. Shelf Res. 28 (12), 1483–1489. https://doi.org/10.1016/j.csr.2007.02.009.

Zhou, Y., Zhang, Y., Li, F., Tan, L., Wang, J., 2017. Nutrients structure changes impact the competition and succession between diatom and dinoflagellate in the East China Sea. Science of the Total Environment, the 574 (C), 499–508. https://doi.org/10.1016/j.scitotenv.2016.09.092.

Zhou, Z.-X., Yu, R.-C., Sun, C., Feng, M., Zhou, M.-J., 2019. Impacts of Changjiang River discharge and Kuroshio intrusion on the diatom and Dinoflagellate blooms in the East China Sea. J. Geophys. Res. Oceans 8 (1). https://doi.org/10.1029/2019JC015158. 39–14.

Zhu, Z.-Y., Ng, W.-M., Liu, S.-M., Zhang, J., Chen, J.-C., Wu, Y., 2009. Estuarine phytoplankton dynamics and shift of limiting factors: a study in the Changjiang (Yangtze River) Estuary and adjacent area. Estuar. Coast. Shelf Sci. 84 (3), 393–401. https://doi.org/10.1016/j.ecss.2009.07.005.

Zhu, Z.-Y., Wu, Y., Zhang, J., Du, J.-Z., Zhang, G.-S., 2014. Reconstruction of anthropogenic eutrophication in the region off the Changjiang Estuary and central Yellow Sea_ from decades to centuries. Cont. Shelf Res. 72 (C), 152–162. https://doi.org/10.1016/j.csr.2013.10.018.